

Physical conditions and redshift evolution of optically thin C III absorbers: Low- z sample

Abhisek Mohapatra^{1*}, R. Srianand², Ananta C. Pradhan¹

¹Department of Physics and Astronomy, National Institute of Technology, Rourkela, Odisha 769 008, India

²Inter-University Centre for Astronomy & Astrophysics, Postbag 4, Ganeshkhind, Pune 411 007, India

Accepted Received ; in original form

ABSTRACT

We present a detailed analysis of 99 optically thin C III absorption systems at redshift, $0.2 \leq z \leq 0.9$ associated with neutral hydrogen column densities in the range, $15 \leq \log N(\text{H I}) (\text{cm}^{-2}) \leq 16.2$. Using photoionization models, we infer the number density (n_{H}), C-abundance ($[C/H]$) and line-of-sight thickness (L) of these systems in the ranges, $-3.4 \leq \log n_{\text{H}}$ (in cm^{-3}) ≤ -1.6 , $-1.6 \leq [C/H] \leq 0.4$, and $1.3 \text{ pc} \leq L \leq 10 \text{ kpc}$, respectively with most of the systems having sub-kpc scale thickness. We combine the low- z and previously reported high- z ($2.1 \leq z \leq 3.3$) optically thin C III systems to study the redshift evolution and various correlation between the derived physical parameters. We see a significant redshift evolution in n_{H} , $[C/H]$ and L . We compare the redshift evolution of metallicity in C III systems with those of various types of absorption systems. We find that the slope of $[C/H]$ vs. z for C III absorbers is steeper compared to the redshift evolution of cosmic metallicity of the damped Ly α sample (DLAs) but consistent with that of sub-DLAs. We find the existence of strong anti-correlation between L vs. $[C/H]$ for the combined sample with a significance level of 8.39σ . We see evidence of two distinct $[C/H]$ branch C III populations (low- $[C/H]$ branch, $[C/H] \leq -1.2$ and high- $[C/H]$ branch, $[C/H] > -1.2$) in the combined C III sample when divided appropriately in the L vs. $N(\text{C III})$ plane. Further studies of C III absorbers in the redshift range, $1.0 \leq z \leq 2.0$ is important to map the redshift evolution of these absorbers and gain insights into the time evolution physical conditions of the circumgalactic medium.

Key words: galaxies: evolution - galaxies: haloes - quasars: absorption lines

1 INTRODUCTION

Galaxies accrete gas from its surrounding regions in order to sustain the star forming activity over long timescales ($\sim \text{Gyr}$) (Fox & Davé 2017). In return, various stellar activities push back the gas into the halo of the galaxy and/or into the circumgalactic medium (CGM) through winds (Heckman et al. 2000; Veilleux et al. 2005; Zhang 2018; Lochhaas et al. 2018). The gas flows around a galaxy provide crucial information on the initial mass function and star formation rate (SFR) history of the host galaxy. So, the measurement of chemical abundances and physical parameters of the CGM gas are essential to explore processes driving the evolution of galaxies. However, it is impossible to detect these inflows/outflows in emission via direct observations with current telescopes. Therefore, these gas flows are usually detected in absorption lines embedded in the spectra of luminous background sources (such as quasars and gamma-ray bursts (GRBs); Ford et al. 2014; Hafen et al. 2020; Ho & Martin 2020). Currently, high-resolution spectrographs have

the ability to trace the inflow/outflow in the intervening galaxies with significant sensitivity and resolve the individual components up to a few km s^{-1} .

Metals observed in quasar spectra originating from galactic haloes (or CGM) around the intervening galaxies are found to evolve with cosmic time (Bergeron 1986; Adelberger et al. 2005; Steidel et al. 2010; Keeney et al. 2017; Tumlinson et al. 2017; Muzahid et al. 2018). In the past few decades, absorption line studies show that the photoionized gas with a temperature of about 10^4 K are ubiquitous throughout the gaseous halo of the galaxies up to impact parameters of $\sim 100 \text{ kpc}$ (Stocke et al. 2013; Werk et al. 2013). Using the low redshift COS-Halos sample, Stern et al. (2016) have shown that for $\sim L_*$ galaxies, the haloes are reservoirs of cool gas with masses in the range $\sim 10^{10} - 10^{11} M_{\odot}$. Despite having ample of CGM surveys using quasar absorption lines, the origin and distribution of halo gas in the CGM is still uncertain. However, it has been shown from several hydrodynamic simulations that the enrichment of heavy elements in the CGM is predominantly due to the galactic winds (Veilleux et al. 2005; McCourt et al. 2015; Muratov et al. 2015). The massive

*Contact e-mail: abhisekphy@gmail.com

superwinds of supernova explosions drive the metal enriched out-flowing gas into the haloes of galaxies. The wind material goes through fragmentation due to thermal instabilities to form clumps of clouds (Field 1965; Thompson et al. 2016). The clump of gas then cools with time and reaches pressure equilibrium with the surroundings (McCourt et al. 2015; Heckman et al. 2017) or become self-gravitating (Dedikov & Shchekinov 2004). Recently, several simulation results also suggest that the condensations under thermal instabilities and fragmentation of cool gas are responsible for forming small cloudlets (sizes \sim pc) in the galactic halos (McCourt et al. 2018; Liang & Remming 2020).

Primarily, Mg II $\lambda\lambda 2976, 2803$ doublet transitions have been used over the years to trace the relationship between metal ions and parent galaxies at low to intermediate redshifts ($0.3 \leq z \leq 2.5$) (Petitjean & Bergeron 1990; Chen et al. 2010; Dutta et al. 2017; Joshi et al. 2017). However, the scenario has drastically changed with the use of other metal ions such as low ionized ions of Si II, C II, Si III, (Narayanan et al. 2005; Herenz et al. 2013; Muzahid et al. 2018; Bouma et al. 2019) intermediate to high ionized ions of Si IV, C IV, O VI, Ne VIII (Chen et al. 2001; Bergeron & Herbert-Fort 2005; Muzahid 2014; Muzahid et al. 2015; Hussain et al. 2017), etc., with the help of high-quality and high-resolution UV spectroscopy.

Measurements of column densities of successive ionization stages of an element is advantageous to infer the ionization parameter (U) (alternatively n_{H}) of photoionized cool absorbing gas with an assumed incident ultraviolet background (UVB) radiation. Additionally, $N(\text{H I})$ of the absorbing gas is further used to constrain the physical parameters accurately. Hence, large surveys of successive ions of heavy elements with additional coverage of H I are potentially essential to identify the underlying mechanism of the stability and origin of the absorbing gas. With large surveys, we wish to capture the broad statistics of absorption systems and study various correlations between the derived physical and chemical parameters. This can further enhance our understanding of the absorbers and provide essential ingredients to perform more realistic hydrodynamic simulations of galaxy formation and the evolution of IGM/CGM.

However, the luxury of finding such idealized absorbing gas sample is limited due to various constraints such as, wavelength coverage of all the ions, blending due to the other ionic transitions, detection limits due to signal to noise ratio (SNR), etc. Mostly, carbon is used as a common tracer of metals associated with H I absorbing gas originating from the IGM/CGM (Cowie et al. 1995; Schaye et al. 2007; Boksenberg & Sargent 2015). The C IV $\lambda\lambda 1548, 1550$ doublet and C II $\lambda 1334$ lie redward to the Ly α emission peak of the quasar making them easily detectable and relatively free from contamination. On the other hand, C III $\lambda 977$ falls inside the Ly α forest usually blended by other higher-order H I Lyman series transitions. Due to difficulty in finding clean C III absorption lines and the dearth of C II detection in the low- $N(\text{H I})$ absorption systems, the physical and chemical properties of these absorbing gas often remain poorly constrained. However, considering ionization state, oscillatory strength, and elemental abundance, the C III line is one of the best and strongest ultraviolet (UV) transition to study the optically thin gas absorbers.

Kim et al. (2016) have produced a systematic survey of optically thin C III absorber sample at high redshift, $2.1 \leq z \leq 3.3$. In Mohapatra et al. (2019) [hereafter, M19], we have analysed this sample using the updated Khaire & Srianand (2019) UVBs to explore the redshift evolution of these C III absorbers. We also emphasized the use of accurate UVB in photoionization (PI)

models and its impact on the derived parameters in M19. We found various interesting correlations and anti-correlations of the inferred parameters. We suggested that the anti-correlation between line-of-sight thickness ($L = N_{\text{H}}/n_{\text{H}}$) and C-abundances ($[C/H]$) can be well explained using a simple toy model where L is driven by the cooling time (t_{cool}) as seen in the fragmentation of clouds due to thermal instabilities (McCourt et al. 2018). The C III absorbing gas studied in M19 are expected to be predominantly originated from the galactic haloes or gas around the galactic discs via inflows or outflows. However, we do not find any confirmed detection of galaxy sources within one Mpc impact parameter in the archival spectroscopic or photometric data.

Motivated by the aforementioned findings of M19, we have further extended our study of the C III absorbers to the low redshift range, $0.2 \leq z \leq 0.9$ to explore whether the C III selected absorbers substantially trace the cool fragmented gas clouds in the CGM. Note that, the C III absorption is expected to be relatively less contaminated by the higher-order H I Lyman series absorption at low- z than at high- z and hence, are more reliable in deriving the metallicity of the gas. To derive the physical and chemical parameters of the low- z C III absorbers, we have used grids of PI models. In the PI models, we have implemented the recently updated Khaire & Srianand (2019) [hereafter KS19] UVBs using quasar spectral index (α) values, $-1.6, -1.8$ and -2.0 to study the uncertainties in the derived parameters. Combining the low- z C III absorbers with the high- z C III absorbers from M19, we present a comparative study of the C III absorbers in a wide redshift range of $0.0 \leq z \leq 3.3$. Note that, we do not find any galaxy association for the high- z C III absorbers in M19. In contrast, the low- z C III absorbers are a part of the COS-CGM survey with at least one galaxy within one Mpc projected distance.

This paper is arranged as follows. In §2, we describe the details of the low- z C III sample. We briefly explain the PI models and present the physical and chemical properties of the low- z optically thin C III absorbers in §3. In §4, we discuss the redshift evolution of various parameters and analyse various correlations between the absorber properties. In §5, we discuss our results and emphasize the need for a large survey of homogeneous optically thin C III absorbers across the redshift range which can be used as an essential tracer of the cool fragmented gas around the CGM. Throughout this study we use Λ CDM cosmology with $H_0 = 70 \text{ km s}^{-1} \text{ Mpc}^{-1}$, $\Omega_{\Lambda} = 0.7$, and $\Omega_m = 0.3$. We denote $[A/B] = \log(A/B) - \log(A/B)_{\odot}$ as the abundances of metals and use solar relative abundances values from Grevesse et al. (2010).

2 DATA

Lehner et al. (2018) [hereafter L18] have produced a catalog of 224 H I-selected absorption systems referred to as COS CGM compendium (CCC) using 335 background quasar spectra. The quasar spectra of this CCC sample have been observed using the *G130M* and/or *G160M* gratings of the *Cosmic Origins Spectrograph* (COS) on the *Hubble Space Telescope* (HST).

There are 152 strong Ly α forest systems (SLFs) detected in the CCC with $N(\text{H I})$ (cm^{-2}) in range, $15.0 \leq \log N(\text{H I}) \leq 16.2$ which is spanning over a redshift range, $0.2 \leq z \leq 0.9$. The absorption systems are systematically analysed by L18 to obtain the Doppler parameters (b), $N(\text{H I})$ and the column densities of other observed heavy elements. They have reported the integrated $N(\text{H I})$ and the column densities of the other metal ions of each absorption system. The complete information on detection and column densities of the

observed ions is provided by L18. The detection of several metal ions along with H I is helpful to constrain the physical parameters of the cool CGM gas absorbers. L18 have reported that the lower column density SLFs trace the diffuse CGM gas as well as their transition phase from the CGM to Ly α forest/IGM. The quasar spectra of the SLFs sample have coverage of the wavelength range of both C II and C III ions which allows us to perform PI modelling as explained in M19.

We extract a total of 99 C III absorption systems from the SLFs in the CCC sample. Out of these 99 C III absorption systems, we find 67 well detected C III systems and 32 systems with detections albeit of having saturated C III profile or blended by other metal line transitions which are considered as lower limit C III systems. Similarly, in case of C II, we have firm detections for 18 systems only whereas for the remaining 81 systems we obtain upper limits. The low- z C III absorption systems have the following flags on the measurement of column density:

- (i) Nine clean systems where we could measure the column densities of both C III and C II.
- (ii) 58 systems with clean detection of C III and upper limits on C II ions.
- (iii) 23 systems where we could obtain lower limits on C III and upper limits on C II ions.
- (iv) Nine systems with clean detections of C II ions and with lower limits on C III ions due to line saturation.

Since the low- z C III sample has about 32% absorbers with lower limits on C III, we use the column densities of other detected metal ions (for e.g., Si III, Si II, O III and O II) to further constrain the n_{H} in our PI models. We find 24 Si III + Si II and 24 O III + O II absorption associated with the low- z C III sample. Hence, we have categorized total 99 low- z C III absorption systems based on observed $N(\text{C III})/N(\text{C II})$ as follows:

(i) **Sample A (SA):** It consists of 51 C III systems which is further divided into two sub-samples on the basis of the presence of other metal ions:

SA1: It consists of nine absorption systems with clean C III + C II detections (for such absorption systems, Col ID (8) on observed $N(\text{C III})/N(\text{C II})$ is denoted by ‘0’ in Table B1). Out of which, seven systems have only C III and C II detection, (IDs 18, 19, 30, 39, 56, 66 and 76 in Table B1) and the other two systems also have Si III and Si II detections (IDs 22 and 35 in Table B1 and B2).

SA2: It consists of 42 absorption systems (shown in Table B2 and B3) with lower limits on observed $N(\text{C III})/N(\text{C II})$ but with the presence of other metal ions (Col ID (8) denoted by ‘-2*’ in Table B1). Out of which, 22 absorption systems have Si III + Si II associations (Table B2) and 24 absorption systems have O III + O II associations (Table B3). There are four absorption systems (marked with superscript ‘*’ on the IDs in Table B2 and B3) which have both Si III + Si II and O III + O II ions associations. For systems in this sample, we could get stringent constraints on n_{H} and other parameters from our photoionization models.

(ii) **Sample B (SB):** It consists of 48 absorption systems which have lower limits on $N(\text{C III})/N(\text{C II})$ without presence of any other metal ion combinations. Out of these 48 absorption systems in SB, we have 39 absorbers with clean C III detections and upper limits on C II. Other nine absorbers in this sample have lower limits on $N(\text{C III})/N(\text{C II})$ due to saturated or blended C III profiles and/or upper limits on C II. Since, the absorption systems in this sample have only lower limits on the observed $N(\text{C III})/N(\text{C II})$ (Col ID (8) denoted by ‘-2’ in Table B1) without the presence of other detected metal ion combinations, we could only derive upper limits

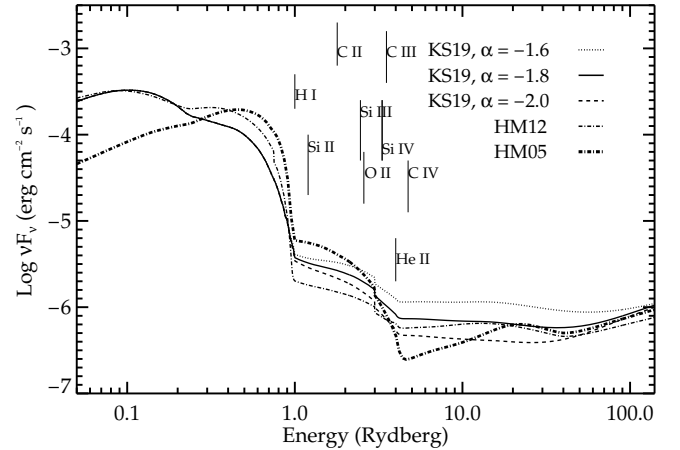


Figure 1. Background spectra predicted by different UVB models at $z = 0.5$ for comparison. The KS19 UVBs with $\alpha = -2.0$, -1.8 and -1.6 are shown using dashed, solid and dotted lines, respectively. We also denote the HM12 and HM05 UVBs with dashed-dotted and thick dash-dotted lines, respectively. The ionization energies of several ions are shown using vertical lines.

on n_{H} and other inferred parameters from our PI models for these absorbers.

3 PI MODELS

We have constructed PI models for C III absorbing gas using the simulation code CLOUDY version c17.02¹ (Ferland et al. 2017). The extragalactic background radiation spectrum of KS19 is inbuilt in this version of CLOUDY and can be included in the model through “table input” command. The basic assumptions in our single phase constant density photoionization models for the absorbing gas are: (i) it has a plane parallel geometry (ii) it is in ionization and thermal equilibrium with an assumed incident UVB radiation and (iii) it has negligible dust depletion. We consider solar relative metallicity measured by Grevesse et al. (2010) which is also the default metal abundances in CLOUDY.

3.1 The UVBs at low- z

The ionization states of metals seen in the CGM/IGM are assumed to be maintained by PI equilibrium with the UVB radiation. In our PI models, we have used the updated KS19 UVB contributed by quasars and galaxies (Q + G) as input ionizing source instead of the frequently used UVBs in the past (i.e., HM05 and Haardt & Madau (2012) (hereafter HM12)). In Fig. 1, we show the KS19 UVB spectra for $\alpha = -1.6$, -1.8 and -2.0 along-with the two HM UVBs (HM05 and HM12 UVBs) at $z = 0.5$. The ionization energies of different ions (such as H I, Si II, C II, Si III, C III, Si IV, C IV, He II, etc.) are marked with vertical lines. As seen in Fig. 1, the KS19 UVBs differ significantly from the HM UVBs due to the different model parameters. The KS19 UVBs exhibit shallower slope in comparison to HM05 UVB between 1.5 – 4 Ryd. Hence, use of HM05 UVB in the PI models as compared to the KS19

¹ CLOUDY version c13.03 (Ferland et al. 2013) was used in M19 for PI models of the high- z absorbers. However, we note that change in CLOUDY version does not alter our inferred results obtained from the PI models.

UVBs will under produce model predicted column densities of ions with ionization potential (IP) in the range, 1.5 – 4 Ryd (e.g., Si IV, C III and C IV) relative to the ions with lower IP (e.g., Si II and C II). [KS19](#) have incorporated the updated quasar emissivity from [Khaire & Srianand \(2015a\)](#) and the SFR density of the low- z galaxies from [Khaire & Srianand \(2015b\)](#). As a result at low- z , the [KS19](#) UVB models have higher H I ionizing photons than the [HM12](#) UVB. Also, the H I PI rates (Γ_{HI}) estimated at low- z using the [KS19](#) UVBs reproduce the measurements of [Shull et al. \(2015\)](#); [Kollmeier et al. \(2014\)](#); [Gaikwad et al. \(2018\)](#) and [Gaikwad et al. \(2017b\)](#) consistently at different redshifts. [KS19](#) have also used the updated $N(\text{H I})$ distribution reported in [Inoue et al. \(2014\)](#) to calculate the opacity of the IGM.

The shape of the UVB mostly relies on (i) the spectral energy distribution (SED) of quasars (basically depends on the value of the spectral index α) and (ii) the escape fraction (f_{esc}) of H I ionizing photons escaping from the galaxies. However, at redshift $z < 1$, the integrated intensity of the UVB (at $E > 13.6$ eV) is mainly dominated by quasars. Hence, the extragalactic UVB radiation at low- z is mostly contributed by quasar SED. The quasar SED is usually calculated by a power law, $f_{\nu} \propto \nu^{\alpha}$, with α values in Far-UV (FUV) are in the range, -0.72 to -1.96 ([Vanden Berk et al. 2001](#); [Telfer et al. 2002](#); [Scott et al. 2004](#); [Shull et al. 2012](#); [Stevens et al. 2014](#); [Lusso et al. 2015](#); [Tilton et al. 2016](#)). Recently, [Khaire \(2017\)](#) has shown that the UVB model with $\alpha = -1.8$ reproduces the He II Ly α optical depth measurements in different redshift ranges (also see [Gaikwad et al. 2019](#)). Hence, we use [KS19](#) UVB with $\alpha = -1.8$ as our fiducial UVB throughout this work. We also calculate the ranges of different cloud parameters [density (n_{H}), metallicity ($[C/H]$), over-density (Δ), and line-of-sight length, ($L = N(\text{H})/n_{\text{H}}$)] considering [KS19](#) UVBs with $\alpha = -1.6$ and -2.0 .

3.2 PI modeling of the low- z C III absorbers

The average gas temperature corresponding to the C III sample obtained from [L18](#) is $T \leq 5 \times 10^4$ K which is estimated from the b parameter of H I absorption. At this temperature, photoionization is the dominant ionization mechanism for these gas absorbers. Hence, the required ionization correction is obtained using the ratio of the column density of metal ions having well-aligned successive ionization stages. The observed column density ratio of two consecutive ionized states of an element (e.g., C II/C III, Si II/Si III, O II/O III etc.) mildly depends on the metallicity but it varies significantly with the shape and intensity of the assumed UVB radiation field, temperature and the density of the absorbing gas ([Lehner et al. 2013](#); [Werk et al. 2014](#); [Hussain et al. 2017](#); [Muzahid et al. 2018](#)). The ionization parameter, U (or n_{H}) of an absorbing gas is constrained by matching the observed column density ratios of successive ionized states of metal ions with the corresponding PI model predicted ratios for an assumed ionizing UVB. Moreover, detection of H I absorption originating from these systems help us to fix the metallicity by matching individual observed column densities heavy elements and $N(\text{H I})$ with the PI model predicted column densities. The necessary initial conditions of PI models for each cloud are: (1) the ionizing UVB, (2) assumed hydrogen density (n_{H}), (3) the stopping criteria and (4) the chemical composition of the gas.

In our PI models, we use the fiducial [KS19](#) UVB (with $\alpha = -1.8$) corresponding to z_{abs} of each absorber as the input ionizing radiation. We use the observed $N(\text{H I})$ for each C III absorption systems as the stopping criteria to terminate the `CLOUDY` computations. We generate grids of PI models for n_{H} , $-5 \leq \log$

n_{H} (cm^{-3}) ≤ -1 , with a grid size of 0.05 dex. Then, we equate the observed column density ratio of the consecutive ionization stages of all the available metal ions (C II/C III, Si II/Si III and O II/O III) with the model predicted column density ratio to uniquely constrain the U (or n_{H}) of the absorber. We use this constrained n_{H} to generate another grid of PI models varying the metallicity $[X/H]$ ($X = \text{C}, \text{Si}$ and O) in the range, $[X/H] = [-2, 0.5]$ (grid size of 0.05 dex). Then we match the individual column densities of respective metal ions (C II, C III, Si II, Si III, O II and O III) with the model predicted column densities to uniquely fix the respective ion abundances (i.e., C-abundance $[C/H]$, Si-abundance $[Si/H]$ and O-abundance $[O/H]$) for an absorption system. We allow `CLOUDY` to determine the kinetic gas temperature self-consistently under PI equilibrium.

The PI models for the sub-sample SA1 are ideal as these systems have clean detections of C III and C II. For SA2, we use other metal ion combinations to put stringent constraint on the derived n_{H} and hence, the n_{H} obtained from these systems are consistent with other observed ion ratios (for e.g., $N(\text{Si III})/N(\text{Si II})$ and/or $N(\text{O III})/N(\text{O II})$) as discussed in the following section. As mentioned in §2, for sub-sample SA (SA1 + SA2), we stress that the physical and chemical parameters obtained using our PI models are well constrained. However, for the sub-sample SB which has 48 lower limit systems, we could only put limits on the derived parameters from our PI models.

3.2.1 Results from the PI models

Here, we discuss about various parameters constrained using our PI models with the fiducial [KS19](#) UVB. Also, we systematically analyse the consistency of the derived parameters of the two sub-samples, SA and SB. We have provided the details of the PI model predicted parameters for all the 99 low- z C III absorption systems in Table B1.

Hydrogen density (n_{H}): In panel (a) of Fig. 2, we have shown the normalized histogram density (NHD) and the cumulative probability density (CPD) distributions of n_{H} for the low- z C III sample in red colour. The n_{H} values for the low- z C III absorption systems derived from the PI models are in the range, $-3.4 < \log n_{\text{H}}$ (in cm^{-3}) < -1.6 , with the mean and median values being -2.45 and -2.48 dex, respectively. Similarly, the n_{H} ranges for the two sub-samples SA and SB are $-3.4 \leq \log n_{\text{H}}$ (in cm^{-3}) ≤ -1.8 and $-3.1 \leq \log n_{\text{H}}$ (in cm^{-3}) ≤ -1.6 , respectively. As the sub-sample SB ($\approx 48\%$ of the absorption systems of the low- z C III sample) has only limits on the column density ratio of $N(\text{C III})/N(\text{C II})$, we could only derive the upper limits on n_{H} for these absorption systems from our PI models. The median n_{H} values of the two sub-samples differ only by 0.14 dex which indicates that the derived n_{H} for both the samples SA and SB are similar. We also notice that 39 systems from SB show similar n_{H} distribution (i.e. considering n_{H} lower limits as detections) like SA with a median density difference of 0.19 dex. We find a median difference of 0.3 dex in n_{H} between our prediction and previously reported values for these absorbers in [Lehner et al. \(2019\)](#) [hereafter L19]. This discrepancy is due to the use of updated UVB in our PI models (see, [Hussain et al. 2017](#), for similar discussions for Ne VIII absorbers). We see that the use of [KS19](#) UVBs with $\alpha = -1.6$ and -2.0 for any absorber causes a maximum uncertainty of 0.34 dex in derived $\log n_{\text{H}}$ values. Hence, we associate an error of ± 0.17 dex in the derived $\log n_{\text{H}}$ for our fiducial model, mostly due to the uncertainty of UVBs irrespective of the observational errors.

For comparison, we have also shown the n_{H} distribution of

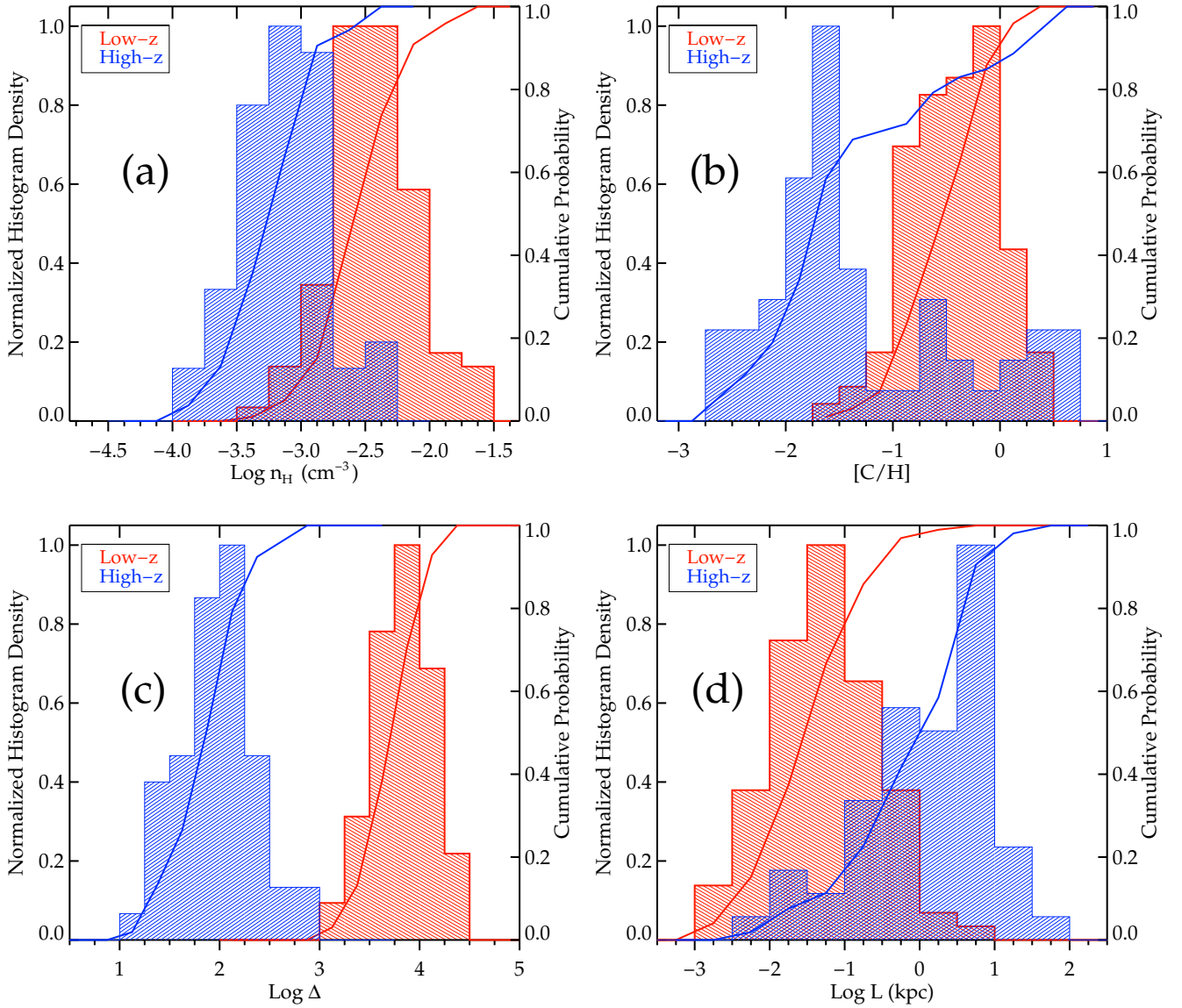


Figure 2. Normalized histogram density (NHD) and cumulative probability distribution (CPD) of derived parameters (n_{H} , $[C/H]$, Δ , and L) of the low- z C III absorption systems obtained using our PI models with the fiducial KS19 UVB. We also show the NHD and CPD of derived parameters for high- z C III system-wide analysed data, S3 (for details of the samples, see M19). We have used red colour for the data analysed in this paper and blue for high- z sample S3 from M19, respectively.

the high- z C III sample (S3) from M19 in panel (a) of Fig. 2 in blue colour. Since we are using total integrated column densities for low- z absorbers, the appropriate comparison will be with the system-wide analysed sample S3 rather than component-wise analysed sample S1 + S2 of M19. As seen in the figure, the peaks of the n_{H} distribution show a significant difference between low- z and high- z C III samples. We perform z-test on the n_{H} distribution of the low- and high- z samples and find that the null hypothesis of the two samples being same is rejected with a negligibly small p-value. This clearly indicates either a redshift evolution of n_{H} between the two samples or different biases in the way the two samples are constructed. The median n_{H} of the low- z C III sample is 0.6 dex higher than the high- z C III systems (S3) in M19. The CPD of n_{H} distributions for the low- z C III sample is also significantly different when compared to the high- z sample S3 of M19.

C-abundance $[C/H]$: The C-abundance $[C/H]$ of each absorption system is obtained by matching the individual column densities of C ions (C II and C III) with the model predicted column densities at a fixed density. However, we have only nine systems (SA1), which have clean detections of C III and C II absorption. So, for most of the absorption systems (for sub-sample SA2 and SB), we have obtained $[C/H]$ by matching the model predicted column density with that of at least one of the observed carbon ion (C III or C II) while making sure the column density of the other ion is consistent with the limiting value obtained from observations. As discussed in the PI models, the different α values (-1.6 and -2.0 in KS19 UVBs) also causes uncertainty of ± 0.12 dex in the measurement of $[C/H]$ with respect to our fiducial KS19 UVB model. The median $[C/H]$ of SA2 (SB) is 0.10 (0.04) dex lower (higher) than the median $[C/H]$ of sub-sample SA1, where we

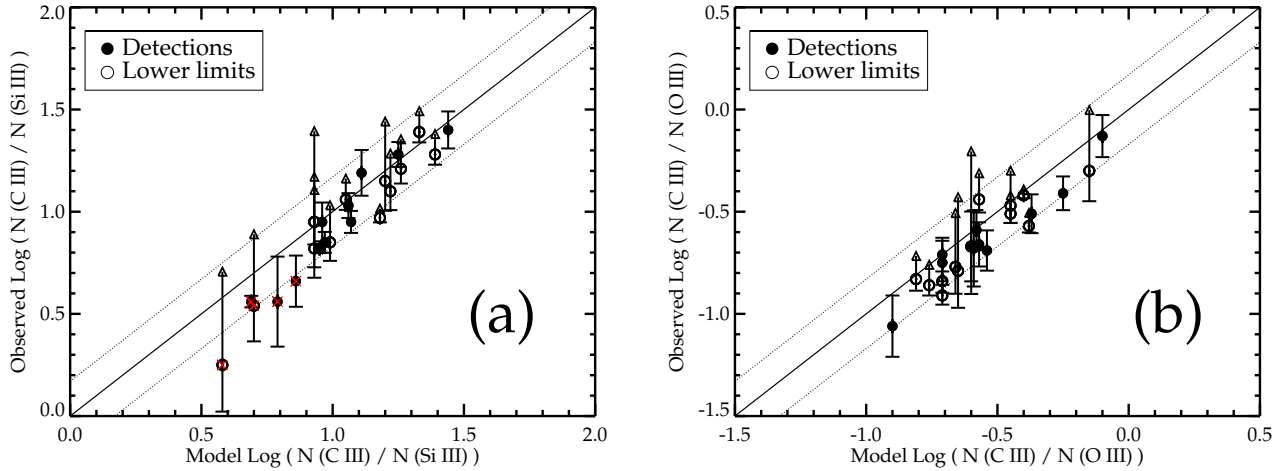


Figure 3. Left panel: Observed $N(\text{C III})/N(\text{Si III})$ is plotted against the model predictions in logarithmic scale. Filled and open circles represent the measurements and lower limits on column density ratios, respectively. The errors in the observed column densities are shown by vertical bars. The solid line represents the ‘ $y = x$ ’ equality line, whereas the dotted line shows the uncertainty range of ± 0.17 dex within this equality line owing to the model uncertainties. Absorbers with super solar $[\text{Si}/\text{C}]$ values ($[\text{Si}/\text{C}] \geq 0.3$) are denoted with red cross marks. Right panel: same as the left panel except for the observed $N(\text{C III})/N(\text{O III})$ is plotted against the model values in logarithmic scale.

have only nine clean $\text{C III} + \text{C II}$ systems. For the two sub-samples SA and SB, the $[\text{C}/\text{H}]$ ranges are, $-1.3 \leq [\text{C}/\text{H}] \leq 0.4$ and $-1.6 \leq [\text{C}/\text{H}] \leq 0.3$ with the median values -0.51 and -0.41 , respectively. We also find that 39 systems with C III detections and limits on C II from SB show identical $[\text{C}/\text{H}]$ distribution as SA with a negligible median difference of 0.06 dex. Hence, we conclude that different sub-samples of low- z C III absorbers show similar $[\text{C}/\text{H}]$ distributions irrespective of sample choices.

As we have n_{H} measurements using other ion ratios for C III systems in SA2 without C II detections, we use the ionization corrections for C III ($f_{\text{C III}}$) and H I ($f_{\text{H I}}$) predicted by the PI models to check the consistency of our derived $[\text{C}/\text{H}]$. In this case, we calculate C-abundance as,

$$[\text{C}/\text{H}] = \log N(\text{C III})/N(\text{H I}) - \log f_{\text{C III}}/f_{\text{H I}} - \log (\text{C}/\text{H})_{\odot} \quad (1)$$

for each absorption system using the observed $N(\text{C III})$ and $N(\text{H I})$. We find that the $[\text{C}/\text{H}]$ obtained using this method is well within error range (± 0.12 dex due to uncertainty in the quasar SED while modeling the UVBs) of the derived $[\text{C}/\text{H}]$ from our PI models with a median difference of 0.05 dex. Thus, even if we have only upper limits for $N(\text{C II})$ for the sub-sample SA2, our PI model inferred $[\text{C}/\text{H}]$ are robust and reliable.

In panel (b) of Fig. 2, we have shown the NHDs and CPDs of $[\text{C}/\text{H}]$ distribution for both the low- z (red) and high- z (blue) samples. The derived $[\text{C}/\text{H}]$ for low- z C III systems is in the range, $-1.6 \leq [\text{C}/\text{H}] \leq 0.4$ with a median value of -0.46 . We find that the overall $[\text{C}/\text{H}]$ distribution for low- z is unimodal. Moreover, the C III selected sample seems to be associated with high metallicity end of its parent SLF sample of L19. The median $[\text{C}/\text{H}]$ of the low- z C III systems is found to be 1.1 dex higher than the high- z C III systems in M19. There are total 14 ($\approx 14\%$) absorption systems in SA + SB, which show super solar C-abundances. Comparatively in M19, there are eight ($\approx 15\%$) super solar C III systems in S3. However, when we restrict ourselves to absorbers with $N(\text{H I}) \geq 10^{15} \text{ cm}^{-2}$ (like the low- z absorbers), we found only one ($\approx 3\%$) super solar system in S3 of M19. This once again is consistent with the fact that the low- z C III absorption systems are more

metal enriched than their high- z counterparts. Kim et al. (2016) suggested a bimodal distribution of metallicity among high- z C III systems. This is also barely apparent in panel (b) of Fig. 2. The $[\text{C}/\text{H}]$ distribution of the low- z C III sample almost lies within the high metallicity branch ($[\text{C}/\text{H}] > -1.4$) of high- z C III systems. Interestingly, we do find the paucity of low metallicity ($[\text{C}/\text{H}] < -1.6$) absorption systems in low- z C III sample despite of having overlapping $N(\text{H I})$ ranges.

Over-density (Δ) and the line-of-sight thickness (L): In panel (c) in Fig. 2, we have shown the NHDs and CPDs of gas over-density parameter ($\Delta = n_{\text{H}}/\bar{n}_{\text{H}}$, where $\bar{n}_{\text{H}} = 1.719 \times 10^{-7} \text{ cm}^{-3} (1+z)^3$ is the mean hydrogen density of the universe). The derived Δ for the low- z C III systems are in range, $\log \Delta \sim 3 - 4.5$, with a median over-density, $\langle \log \Delta \rangle_{\text{median}} \sim 3.74$. The over-densities for these systems clearly confirms that these absorbers do not resemble the physical properties of typical IGM gas and are probably originating from high over-dense regions like CGM.

Hydrodynamical simulations of the low- z Ly α forest at $z \sim 0$ indicate that most of the absorption with $N(\text{H I}) \sim 10^{15} \text{ cm}^{-2}$ and $T < 10^5 \text{ K}$ will be associated with the condensed gas phase and originated from regions with $\Delta \geq 100$ (i.e., $\log \Delta \geq 2.0$) (see Fig. 5 and Fig. 8 of Gaikwad et al. 2017a). The above inferred range in Δ is at least an order of magnitude higher (i.e., $\log \Delta = 3 - 4.5$ for $N(\text{H I}) (\text{cm}^{-2}) = 10^{15} - 10^{16.2}$) than that predicted by Δ vs. $N(\text{H I})$ relationship for the Ly α forest absorbers (see equation 10 of Gaikwad et al. 2017a, and values given in their Table 2). This once again suggests that the C III absorbers may be related to CGM. The median Δ measured for the low- z C III absorbers is 1.6 dex higher than their high- z counterparts. The large difference in Δ as compared to n_{H} is mainly due to the strong redshift dependence of mean density \bar{n}_{H} .

Panel (d) in Fig. 2 shows the NHDs and CPDs of line-of-sight thickness, $L \sim N(\text{H})/n_{\text{H}}$. We find that the L obtained for SA + SB is varying over a large range from 1.3 pc to 10 kpc with a median line-of-sight thickness of 60 pc. The median L of the low- z C III systems is ~ 10 times lower than that measured for the high- z counterparts. As the size of the regions may be related to physical

parameters such as sound speed, cooling time-scale, etc., (see M19), this difference suggests a strong redshift evolution in the physical parameters (like metallicity and density) of the C III absorbers.

PI model predictions for other ions: As discussed earlier, for constraining n_{H} , we consider other metal ions (Si III, Si II, O III and O II) present in the absorbing gas in our PI models. We have presented the constrained $[Si/H]$ and $[O/H]$ for sample SA2 in Table B2 and B3, respectively. In order to show the consistency, we compare the observed column density ratios involving Si III and O III with the PI model predictions. In panel (a) and panel (b) of Fig. 3, we plot the observed column density ratios of $N(\text{C III})/N(\text{Si III})$ and $N(\text{C III})/N(\text{O III})$ against their respective PI model predicted values. The filled circles show detections of the observed ratios whereas the open circles with arrows show the lower limits. The errors in the observed ratios are shown by vertical bars. The solid line represents the ‘ $y = x$ ’ equality line where the observed ratio is exactly equal to the model predicted ratio. The dotted lines indicate uncertainty range of ± 0.17 dex around the ‘ $y = x$ ’ line which arises due to the PI model uncertainties (caused by the UVBs). We found 20 (resp. 17) Si III (resp. O III) detections and 4 (resp. 7) lower limit systems out of the total 24 (resp. 24) Si III + C III (resp. O III + C III) systems in the low- z C III sample. It is seen from Fig. 3 that for all the systems, the observed column density ratios are consistent within the uncertainty range of ± 0.17 dex of the PI model predicted column density ratios. From the above validations, it is quite evident that the n_{H} obtained using observed column densities of Si and O ions are well constrained and consistent. We have also obtained the $[Si/H]$ and $[O/H]$ for all the systems while reproducing the observed column density of C II, C III, Si II, Si III and O II, O III, respectively. The mean $[Si/C]$ and $[O/C]$ of the absorbers are $\sim 0.09 \pm 0.17$ and $\sim 0.31 \pm 0.22$, respectively. The mean $[Si/C]$ in the C III absorbers are close to the solar value whereas mean $[O/C]$ to be super solar. However, for some of the Si III + C III absorbers (marked in red stars in panel (a) of Fig. 3), we find $[Si/C]$ to be super solar and require slight enhancement of $[Si/H]$ in order to produce the observed $N(\text{C III})/N(\text{Si III})$ in our PI models. Further investigations of such absorbers will be explored in a future work.

4 DISCUSSION

4.1 Evolution of physical parameters with redshift

In this section, We discuss redshift evolution of physical parameters, n_{H} , Δ , L , and $[C/H]$ of the low- z C III absorption systems obtained using our PI models with the fiducial KS19 UVB. We use Spearman rank correlation test to study the correlation between different parameters. Since $\approx 48\%$ of the absorption systems in the low- z C III sample (i.e., for sample SB) have limits on the derived parameters, we perform a survival test with ASURV PACKAGE (ASTRONOMY SURVIVAL ANALYSIS PACKAGE) (Lavalley et al. 1992) for the correlation analysis. ASURV package implements the statistical methods for handling censored data with upper limits as presented in Feigelson & Nelson (1985) and Isobe et al. (1986). We have used the bivariate method to determine the correlation between any two derived parameters considering the samples with the limits as the censored sample (see Table 1). ASURV provides generalizations of Spearman’s rank correlation which also allows upper limits in both the variables.

In panel (a) of Fig. 4, we show redshift vs. n_{H} for the low- z C III absorption systems. The n_{H} of the C III systems show an increasing trend with redshift. We find the Spearman rank

Table 1. Correlation analysis of derived parameters using Spearman rank correlation test and survival test with the ASURV package (Lavalley et al. 1992).

Parameters	Spearman Rank correlation		Survival test	
	ρ_s	ρ_s/σ	ρ_s	ρ_s/σ
z vs. $\log n_{\text{H}}$	+0.52	+5.16	+0.33	+3.27
z vs. $[C/H]$	-0.11	-1.08	-0.16	-1.58
z vs. $\log L$	-0.24	-2.33	-0.19	-1.88
z vs. $\log \Delta$	+0.16	+1.58	+0.10	+1.01
$\log L$ vs. $[C/H]$	-0.47	-4.61	-0.39	-3.86
$\log L$ vs. $\log N(\text{C III})$	+0.59	+5.83	+0.52	+5.16
$\log L$ vs. $\log N(\text{H I})$	+0.35	+3.48	+0.28	+2.77
$[C/H]$ vs. $\log N(\text{C III})$	+0.33	+3.27	+0.31	+3.07
$[C/H]$ vs. $\log N(\text{H I})$	-0.44	-4.38	-0.35	-3.47

Table 2. The Kolmogorov-Smirnov (KS) statistics with maximum deviation (D_{KS}) and the probability of finding the difference by chance (p -value) for different redshift bins.

Parameters	L1 vs L2		H1 vs H2		low- z vs high- z	
	D_{KS}	p -value	D_{KS}	p -value	D_{KS}	p -value
n_{H}	0.47	2.23×10^{-5}	0.29	0.52	0.72	4.01×10^{-12}
$[C/H]$	0.09	0.95	0.32	0.32	0.75	3.92×10^{-13}
L	0.36	2.5×10^{-3}	0.38	0.15	0.81	2.82×10^{-15}

correlation coefficient, $\rho_s = 0.52$ with a confidence level of 5.16σ . The sub-sample SA shows correlation coefficient $\rho_s = 0.37$ at a confidence level of 2.65σ whereas SB shows a stronger correlation with $\rho_s = 0.71$ at a confidence level of 4.85σ . Hence, the stronger $\sim 5\sigma$ level correlation observed in the full sample could be due to the presence of lower limit C III systems in SB. While the clean C III absorbers in sub-sample SA (i.e., SA1) do not show any statistically significant correlation between z and n_{H} , we find similar $\rho_s (= 0.51)$ like the full low- z sample albeit of slightly lower significance level (3.33σ) for the sub-sample SA2. The survival analysis for the full low- z sample shows 3.27σ confidence level correlation with $\rho_s = 0.33$ (see Table 1) as seen in the case of SA where we have stringent constraint on the derived n_{H} .

In panel (a) of Fig. 5, we show the cumulative distribution of n_{H} obtained in two redshift bins (L1: $0.2 \leq z < 0.45$ and L2: $0.45 \leq z < 0.9$) for the low- z C III absorbers. We provide the Kolmogorov-Smirnov (KS) statistics with maximum deviation (D_{KS}) and the probability of finding the difference by chance (p -value) for different redshift bins in Table 2. A two-sided KS test on n_{H} distributions of the low- z bins shows a maximum difference between the cumulative distributions, $D_{\text{KS}} = 0.47$ and p -value, $p = 2.23 \times 10^{-5}$. It confirms that n_{H} shows a mild increasing trend with redshift for $z \leq 0.9$. As discussed in §3.2.1, the n_{H} range obtained at high- z is lower than the n_{H} range measured at low- z . A two-sided KS test also indicates statistically significant difference ($D_{\text{KS}} = 0.72$ and $p = 4.01 \times 10^{-12}$) in n_{H} distribution between low- z and high- z C III absorbers (see Table 2). We have also divided the high- z C III sample of M19 into two redshift bins (H1: $2.0 \leq z < 2.5$ and H2: $2.5 \leq z < 3.3$). From panel (a) of Fig 5, we see that there is no clear n_{H} dependence of z between these two high- z redshift bins. Thus, our analysis suggests that the redshift evolution of n_{H} for C III absorbers is not monotonic. Interestingly this trend we notice is very much similar to the redshift dependence of Γ_{HI} in the KS19 UVBs (see Fig. 4 of Khaire & Srianand 2019). We discuss this further in §4.1.1.

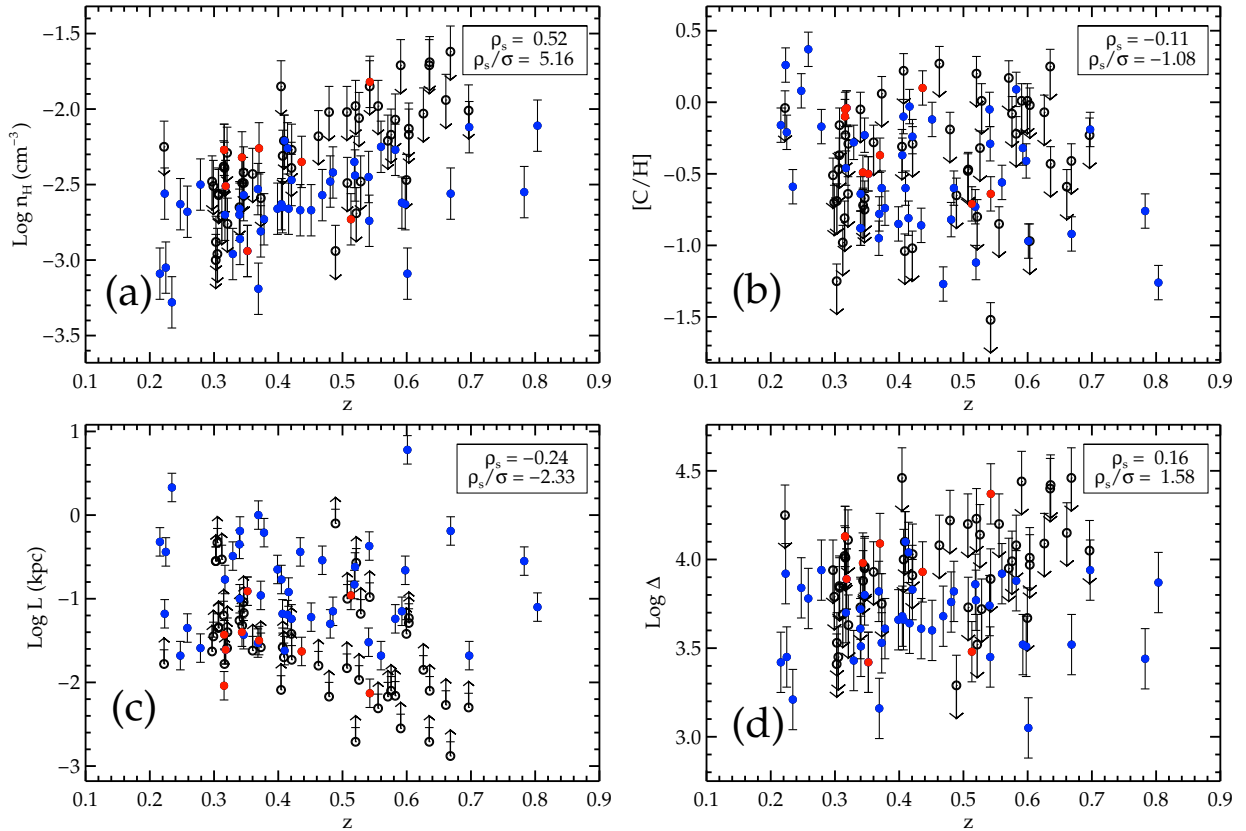


Figure 4. The redshift evolution of the model predicted parameters, hydrogen density (n_{H}), metallicity (C/H), line-of-sight thickness (L) and over-density (Δ) are shown along with their respective rank correlation coefficients and significance levels. The red and blue solid circles with error bars represent the sub-samples, SA1 and SA2, respectively, whereas, the open circles with arrows show the limit on the derived parameters for SB.

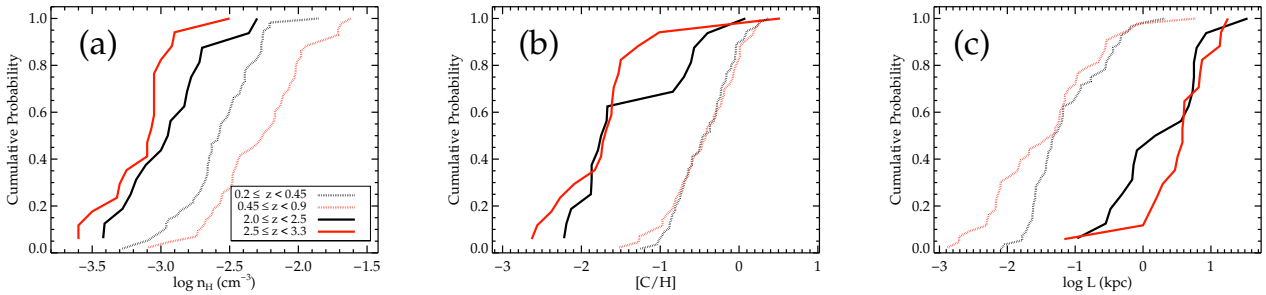


Figure 5. Redshift evolution of derived physical parameters, n_{H} (panel (a)), $[C/H]$ (panel (b)) and L (panel (c)) for the high- z (solid lines) and low- z (dotted lines) C III sample. Black and red lines as shown in the legends in panel (a) represent the different redshift bins used in respective redshift ranges.

We show $[C/H]$ as a function of z in panel (b) of Fig. 4. For the low- z C III absorption systems, $[C/H]$ lacks a clear trend with z , and we find $\rho_s = -0.11$ with a confidence level of 1.08σ . The survival test also confirms the same with similar $\rho_s = -0.16$ at a slightly higher significance level of 1.58σ . The commutative distributions for L1 and L2, as shown in panel (b) of Fig. 5 also confirms the same. As seen from Table 2, the two-sided KS test gives $D_{KS} = 0.09$ with a high p-value. The large spread in $[C/H]$ distribution for the low- z sample indicates that these absorbers probably trace the CGMs of different types of host galaxies. Note that, in our analysis of C III selected absorbers, $[C/H]$ solely depends on the column densities of C ions and hence, it is slightly different from the metallicity reported in L18. Similar to n_{H} , we find

a strong redshift evolution of $[C/H]$ between low- z and high- z C III absorbers of M19 which is also confirmed using a two-sided KS test indicated in Table 2 ($D_{KS} = 0.75$ with a p-value 3.92×10^{-13}). However, we do not see such strong redshift evolution of $[C/H]$ within small redshift intervals for both the cases of the low- z and high- z C III absorbers. This suggests that metallicity in the CGM evolves slowly with redshift. In §4.4, we compare the redshift evolution of metallicity seen in C III systems with other types of quasar absorption systems.

In panel (c) of Fig. 4, we plot L vs. z . We find a mild redshift evolution of L with redshift ($\rho_s = -0.24$ at a significance level of 2.33σ). The survival analysis test confirms the same with $\rho_s = -0.19$ at 1.88σ level. Panel (c) of Fig. 5 and K-S test from Table 2

also confirm the shallower trend in L as a function of z for the low- z C III absorption systems. This mild correlation is mainly due to the lower limit absorbers of sub-sample SB. We see a large spread in L within small intervals of redshift which suggests that the low- z C III absorbers are tracing in-homogeneously mixed population of pc to sub-kilo parsec scale absorbers in the CGM. However, when we compare our L measurements with those of M19 we do see a statistically significant evolution in L with z (see panel (c) of Fig. 5). A two-sided KS test on L for the low- z and high- z samples gives $D_{KS} = 0.81$ and $p = 2.82 \times 10^{-15}$, implying a significant difference in L distributions. It is also clear from this figure that the L distributions are similar for the two high- z bins ($D_{KS} = 0.38$ and $p = 0.15$) compared to a slight different distributions of L between the two low- z bins ($D_{KS} = 0.36$ and $p = 2.5 \times 10^{-3}$). The median L of the entire low- z sample is ~ 51 pc whereas the median L of the sub-sample SA and SB are ≈ 75 pc and ≈ 31 pc, respectively. We see similar C III systems having sub-kilo parsec scale line-of-sight length predominantly present at $z \sim 2.1 - 2.5$ as reported in M19. However, the frequency of occurrence of such systems is only 15% at high- z . Interestingly, when we consider absorbers with $N(\text{H I}) \geq 10^{15} \text{ cm}^{-2}$, we find only 6% of these high- z C III absorbers with sub-kpc scale line-of-sight thickness.

In panel (d) of Fig. 4, we plot the redshift evolution of Δ for the low- z C III absorption systems. We do not see any statistically significant correlation between these two for the low- z C III sample in contrary to the strong correlation found for high- z C III sample of M19. As seen in panel (a) of Fig. 4, there is a positive correlation between n_{H} and redshift and also, there is a strong dependence of $\overline{n_{\text{H}}}$ on z as, $\overline{n_{\text{H}}} = 1.719 \times 10^{-7} \text{ cm}^{-3} (1+z)^3$. Hence, Δ becomes almost independent of z for low- z C III sample. The survival test also confirms the same with $\rho_s = 0.10$ at a significance level of 1.01σ . The lack of redshift evolution of n_{H} and Δ is generally expected if the C III absorbers predominantly originate in the CGM of galaxies. In this case, the n_{H} distribution is dominated by the prevailing local physical conditions and not from the cosmological density fluctuation (as in the case of Ly α absorption from the IGM).

4.1.1 UVB and density evolution with z :

In §4.1, we have discussed about the evolution of n_{H} as a function of z . We notice that the inferred evolution is not monotonous and to some extent seems to follow the redshift evolution of the UVB. It is also important to remember while we use $N(\text{C III})/N(\text{C II})$ to measure n_{H} at low- z , at high- z , we preferred $N(\text{C IV})/N(\text{C III})$ instead. The difference in choice is purely due to observational constraints. So, in order to study the UVB and n_{H} evolution in a large redshift range, we have therefore combined the low- z (0.2 – 0.9) sample with the previously analysed high- z (2.1 – 3.3) sample from M19 for the absorbers having $N(\text{H I}) \geq 10^{15} \text{ cm}^{-2}$.

In top panel of Fig. 6, we show the variation of observed $N(\text{C III})/N(\text{C II})$ vs. z using scattered circles. The red and blue circles represent the low and high redshift data, respectively. We have obtained $N(\text{C II})$ for the high- z C III systems from Kim et al. (2016). We have estimated the upper limits using apparent optical depth method from the spectra for some of the absorbers where C II was not reported by Kim et al. (2016). We have divided the entire redshift range into four redshift bins, [0.2, 0.45], [0.45, 0.9], [2, 2.5] and [2.5, 3.3]. The ranges of observed $N(\text{C III})/N(\text{C II})$ in logarithmic scale corresponding to the above redshift bins are, [-0.34, 0.93], [-0.55, 1.38], [0.21, 2.52] and [0.20, 2.31], respectively. The filled stars indicate the median observed $N(\text{C III})/N(\text{C II})$ (0.36, 0.24, 1.24 and 1.35) at each median value of the four redshift bins (0.35, 0.58, 2.37

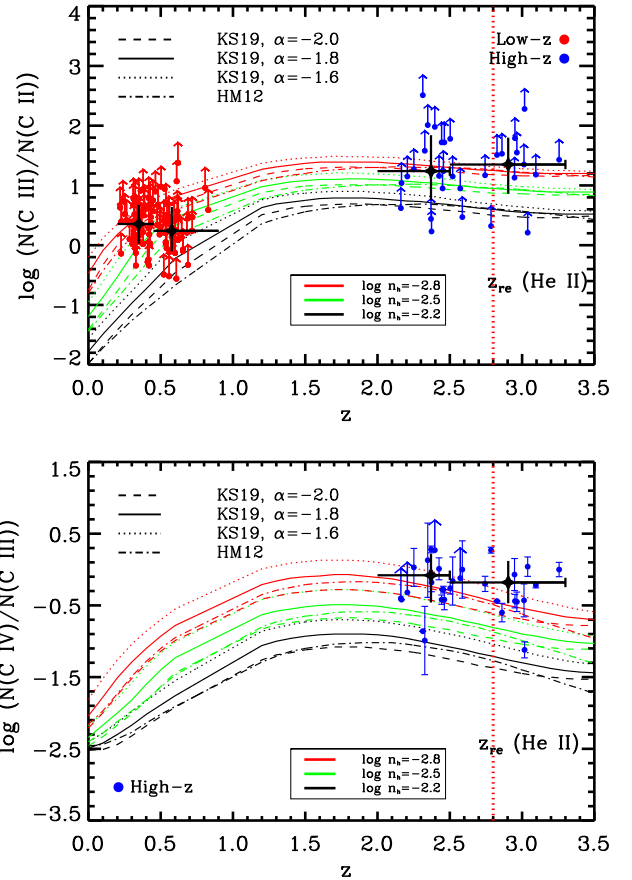


Figure 6. Top panel: The observed $N(\text{C III})/N(\text{C II})$ for low- z and high- z C III systems versus redshift. The red and blue circles represent the low- and high- z data, respectively. The thick stars denote the median value of the observed ratio obtained over the extent of each horizontal bar in the redshift range with the vertical bar showing the 1σ range in the median values. The model predicted column density ratios obtained using different UVBs (KS19 UVBs for α , -1.6, -1.8 and -2.0 and HM12 UVB) are over-plotted using different lines as shown in the legends. From bottom to top, n_{H} is decreasing as denoted by the legends. The vertical red line shows the reionization redshift (z_{re}) of He II obtained using KS19 UVB (Khaire 2017). Bottom panel: The observed $N(\text{C IV})/N(\text{C III})$ for the low- and high- z C III systems versus redshift. Symbols and colours are same as the top panel. Note that the lack of C IV at low- z is just observational bias. Hence, we use the model curves obtained with the median density ($\log n_{\text{H}} \approx -2.5$) of the low- z C III absorption systems along with the 1σ ranges ($\log n_{\text{H}} \approx -2.8$ and -2.2).

and 2.91), respectively. The median observed $N(\text{C III})/N(\text{C II})$ show a mild variation within small redshift ranges (0.2–0.9 and 2.1–3.3) which again indicates a slower evolution of C III absorbers in the CGM as discussed in §4.1. However, the median $N(\text{C III})/N(\text{C II})$ for low- z absorbers is approximately ≈ 1.2 dex lower than the high- z counterparts which may drive the observed n_{H} evolution at low- z .

To further investigate this, we run a set of constant n_{H} PI models using different UVBs (KS19 UVBs ($\alpha = -1.6, -1.8$ and -2.0) and HM12 UVB) assuming a constant temperature and metallicity of 2×10^4 K and 0.1 Z_{\odot} , respectively. The stopping criteria for the PI model is set at $(N(H))$ for an assumed n_{H} and taken from Schaye (2001) as, $N(H)_J \sim 1.6 \times 10^{21} \text{ cm}^{-2} n_{\text{H}}^{1/2} T_4^{1/2} \left(\frac{f_{\text{g}}}{0.16} \right)^{1/2}$, where,

$T_4(K) = T(K)/10^4$ and f_g is the gas mass fraction. We have used $f_g = 0.16$ to evaluate the stopping criteria $N(H)_J$ for each n_H values. We have generated grids of column densities of observed ions in the redshift range, 0 to 3.3 (with a step size of 0.1) for n_H in range, $-1.0 \leq n_H \leq -4.0$ (with a step size of 0.05). Note that, this assumption is valid for deriving the physical parameters of typical IGM Ly α absorbers and are simple enough to explain the UVB evolution and n_H variation due to the UVBs (for a brief discussion see, Section 3.2 of M19). Here, the model curves may not predict the true physical n_H of the C III absorbers as derived in our fiducial PI models.

The model generated $N(\text{C III})/N(\text{C II})$ for three n_H values (median n_H ($\log n_H = -2.5$; green) of the low- z absorbers along-with the 1σ ranges ($\log n_H = -2.8$; red and -2.2 ; black)) are over plotted in the top panel of Fig. 6 with different line styles as shown in the legends. It is clear from this figure that for a given n_H the model predicted $N(\text{C III})/N(\text{C II})$ is almost one dex lower at $z \approx 0.5$ than at $z \approx 2.5$ with a steeper slope for $z \leq 1.2$. As discussed above, the median observed $N(\text{C III})/N(\text{C II})$ in low- z bins are almost constant in the low- z range, $0.2 \leq z \leq 0.9$. Therefore, this nearly constant $N(\text{C III})/N(\text{C II})$ observed for $z \leq 0.9$ will require n_H to increase mildly with increasing z . As seen from this figure, the range of n_H that explains the low- z points under predict $N(\text{C III})/N(\text{C II})$ at high- z . Hence, for a given UVB, one has to decrease n_H values compared to that at low- z . It is also evident that this difference can not be accommodated using the change in α (i.e., the quasar SED in the UV range used in the UVB calculations).

Next, to check whether $N(\text{C IV})$ to $N(\text{C III})$ predict the same n_H evolution, we show the variation of observed $N(\text{C IV})/N(\text{C III})$ with redshift in bottom panel of Fig. 6. Note that, at low- z ($0.2 \leq z \leq 0.9$) the C IV is not observable owing to the limitation of *HST/COS* wavelength coverage. We have also over plotted the model predicted $N(\text{C IV})/N(\text{C III})$ for the same n_H ranges as discussed above for different UVBs indicated by different line-styles as shown in the legends. It is evident from the figure that the high- z $N(\text{C IV})/N(\text{C III})$ will also require slightly lower n_H values as suggested by $N(\text{C III})/N(\text{C II})$. So for a given UVB, the n_H needs to be changed for C III absorbers at low- z compared to high- z but not in a monotonically way in order to yield the observed column density ratios.

There are few possible biases that could have lead to the n_H evolution we note here. The low- z sample typically has higher $N(\text{H I})$ compare to the high- z sample. In cosmological simulations one finds absorption from a given $N(\text{H I})$ originating from higher densities at low- z . The n_H values discussed here are for a system, i.e., averaged over different individual velocity components. Also, our measurements assume a single phase for C II, C III, and C IV. Therefore a better picture will emerge if we can do the analysis of individual components over the full redshift range including addition data of C III absorbers at $1.0 \leq z \leq 2.0$.

4.2 Correlations between derived parameters:

In M19, we have studied the correlations between different derived parameters of C III absorbers for component-wise analysed data (S1 + S2) and system-wide analysed data (S3), separately (see Fig. 10 of M19). We found an interesting anti-correlation between L and $[C/H]$ with significance level, 6.1σ and 3.8σ for S1 + S2 and S3, respectively. We explain this anti-correlation using a simple toy model where L is driven by the cooling length scale ($t_{cool} \times c_s$) as seen in the cloud fragmentation under thermal instabilities (McCourt et al. 2018).

In Fig. 7, we show the correlations between various derived parameters of the low- z C III absorption systems (indicated by circles). We also have over-plotted the same parameters of high- z C III sample, S3 from M19 (indicated by squares) in order to make a comparative correlation analysis. In each panel, the redshift value increases with the symbol size, for the systems of respective samples.

4.2.1 L vs. $[C/H]$:

In panel (a) of Fig. 7, we show the anti-correlation between L and $[C/H]$ for the low- z sample (filled circles) with colour coded n_H values as displayed in the side colour bar. For the low- z C III absorption systems, we see an anti-correlation in L vs. $[C/H]$ with Spearman rank correlation coefficient, $\rho_s = -0.47$ at 4.61σ level (see, panel (a) of Fig. A1 for L vs. $[C/H]$ of the low- z sample only). The survival analysis test also confirms the anti-correlation between these two parameters with $\rho_s = -0.39$ at a significance level of 3.86σ (see Table 1). Muzahid et al. (2018) have noted a similar correlation in their $z < 0.3$ COS-weak sample. We also plot the data from high- z C III sample, S3 from M19 (open squares) in Fig. 7. As shown in the figure, the low- z C III absorption systems are skewed towards the high- $[C/H]$ and low L , whereas the high- z C III sample has a wider spread in $[C/H]$ and L . In the overlapping metallicity range (i.e., $[C/H] \geq -1.2$) the low- z absorbers tend to have smaller L than the high- z counterparts. It is also evident from the figure that the low- z systems with smaller L also have higher n_H . We observe a strong anti-correlation in L vs. $[C/H]$, with Spearman rank correlation value $\rho_s = -0.69$ significant at 8.39σ level, for the combined sample of the low- z and high- z C III absorption systems. To show the strong correlation, we have also plotted linear regression fit (LRF) with 1σ range using black solid and dashed lines in Fig. 7. We obtain a strong dependence of L on $[C/H]$ as:

$$\log L = (-1.49 \pm 0.07) + (-0.93 \pm 0.08)[C/H]. \quad (2)$$

The LRF for the combined sample has a steeper slope compared to the low- z C III sample ($\log L = (-1.60 \pm 0.10) + (-0.78 \pm 0.15)[C/H]$). It is also evident that the size of the absorption system for a given $[C/H]$ is typically smaller for low- z . This also implies that the actual sizes of the low- z absorbers are smaller than the predictions of the toy model used by M19 for modelling this correlation at high- z . Furthermore, we find that for the combined C III absorbers, the correlation remains unchanged ($\rho_s = -0.68$ with 7.78σ) even if we restrict the high- z sample to SLFs only ($N(\text{H I}) > 10^{15} \text{ cm}^{-2}$).

4.2.2 L vs. $N(\text{C III})$:

In panel (b) of Fig. 7, we plot the observed $N(\text{C III})$ vs. L with the same symbols and colours as mentioned above. For the low- z C III sample, we find a tight correlation between these two parameters with $\rho_s = 0.59$ at 5.83σ (see, panel (b) of Fig. A1) which is also confirmed using a survival analysis test as shown in Table 1 ($\rho = 0.52$ at 5.16σ). However, high- z data points typically have larger L for a given $N(\text{C III})$.

While analyzing similar plot of L vs $N(\text{C IV})$, Kim et al. (2016) argued for the presence of two population based on metallicity. Following similar logic we divide the combined sample into high- $[C/H]$ metallicity ($[C/H] \geq -1.2$ and $\log L < -0.6$) and low metallicity absorbers ($[C/H] < -1.2$ and $\log L \geq -0.6$).

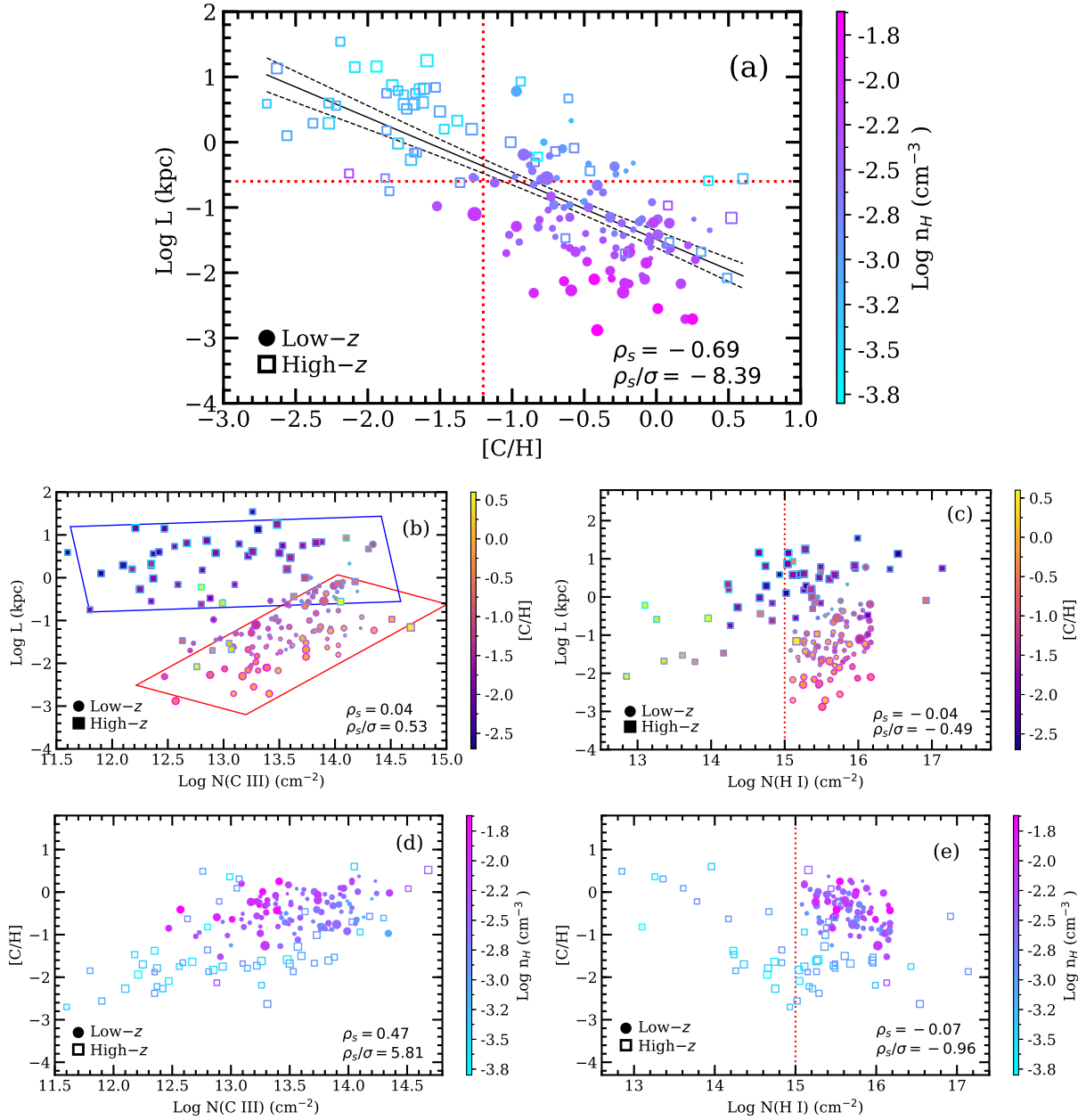


Figure 7. The plots show correlations among various model predicted parameters along with their rank correlation coefficients and significance levels. Panel (a): L vs. $[C/H]$ and the symbols are colour coded with n_H values as shown in the side colour bar. The solid line represents the linear regression fit to the data, whereas the dashed lines indicate 1σ deviation around the linear regression fit. The dotted horizontal and vertical lines show segregation between high- $[C/H]$ ($[C/H] \geq -1.2$ and $\log L < -0.6$) and low- $[C/H]$ ($[C/H] < -1.2$ and $\log L \geq -0.6$) branch C III absorbers (see text for details). Panel (b): L vs. $N(\text{C III})$ with the face of the symbol colour coded with n_H values similar to panel (a) whereas the thick outer lines are colour coded with the $[C/H]$ values as shown with the side colour bar. The regions marked by red and blue boxes show the high- $[C/H]$ and low- $[C/H]$ branch absorbers, respectively.; Panel (c): L vs. $N(\text{H I})$ and the symbols represent same colour coding as panel (b). The vertical red line show $N(\text{H I})$ cut off at $\log N(\text{H I})$ (cm^{-2}) ≥ 15 . The panels (d) and (e) show the $[C/H]$ vs. $N(\text{C III})$ and $[C/H]$ vs. $N(\text{H I})$, respectively, with the side colour bars representing $\log n_H$ values embedded in the symbols. The solid circles and squares represent the parameters corresponding to low- z ($0.2 \leq z \leq 0.9$) and high- z (M19; $2.1 \leq z \leq 3.3$) samples, respectively. The symbol sizes increase with the increasing of redshift within the specified redshift range.

From the boxes drawn in panel (b) of Fig. 7, we find a clear segregation of high- $[C/H]$ (red box) and low- $[C/H]$ (blue box) systems in the L vs $N(\text{C III})$ plane. We see that the high- $[C/H]$ branch absorbers show a clear trend of increasing L with increasing $\log N(\text{C III})$ whereas such a trend is missing for the low- $[C/H]$ branch absorbers with $\log L > 0.4$ kpc. As a result, two distinct

populations in C III sample on the L vs. $N(\text{C III})$ plane are visible in the combined sample with the low- z C III sample following the L vs. $N(\text{C III})$ evolution of high- $[C/H]$ branch of the high- z C III absorbers. While this is in line with the discussions presented in Kim et al. (2016), in our sample the low- $[C/H]$ branch is predominantly dominated by the high- z systems and high- $[C/H]$

by the low- z systems. Hence, it will be interesting to increase the number of C III selected absorbers (spanning a broader range in L and metallicity, $[C/H]$) to confirm the existence of statistically significant bimodality in metallicity among the C III absorption systems.

4.2.3 L vs. $N(\text{H I})$:

We show the correlation between L and $N(\text{H I})$ in panel (c) of Fig. 7. The low- z and high- z C III sample have significantly different $N(\text{H I})$ distributions with $N(\text{H I})$ in ranges, $12.8 \leq \log N(\text{H I}) (\text{cm}^{-2}) \leq 16.6$ and $15 \leq \log N(\text{H I}) (\text{cm}^{-2}) \leq 16.2$, respectively. In the low- z C III sample, all the absorption systems have $N(\text{H I}) \geq 10^{15} \text{ cm}^{-2}$ compared to only $\approx 63\%$ of the high- z absorption systems. Similarly, the size distribution of the absorption systems are different with most of the low $N(\text{H I})$ high- z absorbers showing similar L as the low- z absorbers. Hence, as seen in the figure the low- z and high- z C III absorption systems are separable and have two different distributions on the L vs $N(\text{H I})$ plane. We find a statistically significant correlation between L and $N(\text{H I})$ for the low- z C III sample with $\rho_s = 0.35$ (3.48σ) (see, panel (c) of Fig. A1). The low- z C III absorption systems are skewed towards the lower right end of the L vs. $N(\text{H I})$ plane whereas the high- z C III absorption systems have a larger spread in $N(\text{H I})$ and L and show a stronger correlation with $\rho_s = 0.52$ at 3.48σ . In addition, it is also clear from the figure that analogous of some of the highest metallicity absorbers with smaller L originating from low $N(\text{H I})$ systems are not probed in the low- z sample. For the combined low- z and high- z C III systems, no correlation between L and $N(\text{H I})$ ($\rho_s = -0.04$ at 0.49σ) was found as anticipated based on well displayed segregation.

4.2.4 $[C/H]$ vs. $N(\text{C III})$:

In panel (d) of Fig. 7, we show $[C/H]$ as a function of $N(\text{C III})$ for all the systems. For the low- z C III sample, we see a moderate correlation with $\rho_s = 0.33$ (3.27σ) (see, panel (d) of Fig A1) which is also confirmed from the survival analysis test with $\rho_s = 0.31$ (3.07σ). The high- z sample has a large scatter in $N(\text{C III})$ compared to the low- z sample and shows a strong correlation with $[C/H]$ ($\rho_s = 0.56$ (4σ)). It is also evident from the figure that for a given $N(\text{C III})$, the low- z C III absorbers have systematically higher $[C/H]$ compared to high- z absorbers. This is mainly due to the redshift evolution of metallicity among the C III absorbers as we have discussed in §4.1.

4.2.5 $[C/H]$ vs. $N(\text{H I})$:

We show $[C/H]$ as a function of observed $N(\text{H I})$ for the low- z and high- z absorbers in panel (e) of Fig. 7. We find an anti-correlation between these two quantities with $\rho_s = -0.44$ (at 4.38σ) for the low- z C III absorbers as shown in panel (e) of Fig A1. A survival analysis test also confirms the trends with a $\rho_s = -0.33$ at 3.27σ significance. Note that, this trend is weak compared to the low- z survey of the COS-Halos sample of Prochaska et al. (2017) ($\rho_s = -0.69$ at 3.80σ) and the COS-weak sample of Muzahid et al. (2018) ($\rho_s = -0.94$ at 5.24σ). The high- z C III absorbers over plotted on panel (e) of Fig. 7 also show a weak anti-correlation ($\rho_s = -0.34$ at 2.49σ) with most of the lower- $N(\text{H I})$ absorbers ($N(\text{H I}) \leq 10^{14} \text{ cm}^{-2}$) having $[C/H] > -0.5$ and higher- $N(\text{H I})$ absorbers ($N(\text{H I}) > 10^{14} \text{ cm}^{-2}$) having large scatter in $[C/H]$ in

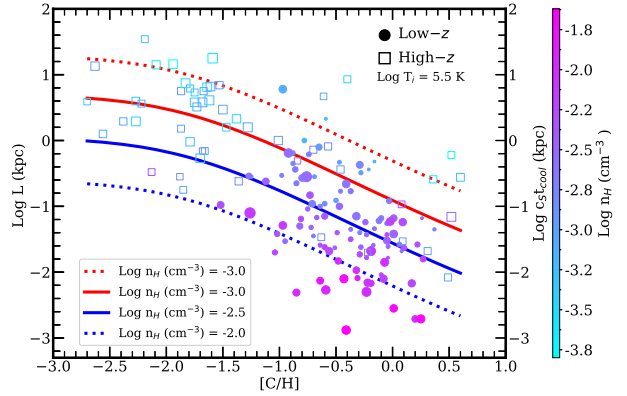


Figure 8. Comparison of L vs. $[C/H]$ of the combined C III systems for a simple isochoric cooling case. The symbols and colours are same as panel (a) of Fig. 7. The cooling length scale ($c_s \times t_{cool}$) obtained from our simple toy model with different constant n_{H} (i.e., for the median n_{H} of low- z ($\log n_{\text{H}} \approx -3$) and high- z ($\log \approx -2.5$) with 1σ upper and lower range, respectively) are indicated with continuous lines as shown in the legends. We use an initial temperature, $\log T_i$ (K) = 5.5 in our model.

the range, $-2.8 < [C/H] < 0.6$. However, a strong anti-correlation was observed between $[C/H]$ and $N(\text{H I})$ ($\rho_s = -0.65$ at 5.80σ) for the component-wise analysed data, S1 + S2 of M19. Hence, the weak trend of C III absorption systems could be due to the possibility of poor small scale metal mixing so that the low-ionization metal lines need not necessarily be associated with the entirely observed $N(\text{H I})$ (for e.g., Schaye et al. 2007). Also, the high- z C III sample on $N(\text{H I})$ vs. $[C/H]$ plane gives a strong hint of metallicity evolution for weak $N(\text{H I})$ ($N(\text{H I}) < 10^{15} \text{ cm}^{-2}$) absorbers. These absorbers are believed to be transients caught in the act and maybe related stripping of metal enriched gas from galaxies or galactic outflows (Schaye et al. 2007). These absorbers seem to be present in group environments and are less active at a later Universe than they were earlier (Muzahid et al. 2018). A homogeneous sample of such absorbers at low and intermediate redshift could shed light to the detail physical process of such transient absorbers in the CGM.

4.2.6 Summary

We find a strong correlation between L and $[C/H]$ for the low- z C III absorption systems as seen in high- z absorbers. However, the low- z and high- z absorbers show different ranges in L and $[C/H]$ for similar $N(\text{H I})$. This means, if L is related to the cooling length ($t_{cool} \times c_s$) as argued by M19, the higher density and metallicity could be the reason for the small L seen in the low- z absorbers having same $N(\text{H I})$. We also notice that the trend seen in the L vs $N(\text{C III})$ plane is consistent with the two population idea suggested by Kim et al. (2016). We find when appropriately divided in L and $[C/H]$ ranges, the high metallicity branch exhibits a correlation between L and $N(\text{C III})$, while the low metallicity branch does not show such correlation. Unfortunately, in the combined sample, low metallicity range (resp. high metallicity range) is dominated by the high- z (resp. low- z) absorbers. Confirming this with an increased number of C III absorbers spanning the L and $N(\text{C III})$ phase uniformly will have interesting implications in understanding the metallicity evolution of CGM gas.

4.3 Size metallicity relationship

The strongest correlation we notice in our study is the one between L vs. $[C/H]$. While this correlation is seen for both high- z and low- z samples, the slopes of the distributions are different. In particular for a given metallicity, L is smaller for low- z systems as these systems tend to have higher n_{H} compare to the high- z systems. In M19, this correlation is explained through a simple toy model where the cloud size is decided by the cooling length.

To explore this further, we obtained $t_{\text{cool}} \times c_s$ for the ‘isochoric’ case with our simple toy model as discussed in M19. In Fig. 8, we show the PI model predicted $[C/H]$ vs. L in scattered points with over plotted ‘isochoric’ model predictions of $t_{\text{cool}} \times c_s$ for different n_{H} (i.e., for the median n_{H} of low- z ($\log n_{\text{H}} \approx -3$) and high- z ($\log \approx -2.5$) with 1σ upper and lower range, respectively). We use an initial temperature, $\log T_i$ (K) = 5.5 in our model. As shown in M19, the model curves roughly follow the observed anti-correlation between $[C/H]$ vs. L for the high- z .

The slight enhancement in n_{H} at low- z explains that the size of the low- z absorbers is less than that of the high- z absorbers for a given metallicity. However, for the low- z , the observed slope is steeper than what is predicted by the model. This is mainly due to the presence of small size clouds near solar metallicity. Also for a given metallicity the predicted range in L is narrower than what we observe. In our toy model, to increase the slope, we have to decrease the cooling time for high metallicity gas. This can naturally happen if we introduce a correlation between the initial density and metallicity in our models. In our data, we do see a moderate (i.e., 2σ) correlation between n_{H} and $[C/H]$. Another possibility is the fragmentation of a larger high metallicity parent cloud to reach pressure equilibrium with its surroundings at a final cooling time scale (McCourt et al. 2018). However, it is important to remember that in this work, we use total column densities (and not the column densities measured for individual components) to derive n_{H} , $[C/H]$ and L . Thus, the inferred length can also be related to the number of individual components along the line-of-sight.

4.4 Redshift evolution of $[C/H]$

Understanding the redshift evolution of metallicity of a particular class of absorption systems (like damped Ly α systems (DLAs) and metal line systems) is very important as it is intimately related to the redshift evolution of star formation and associated feedback processes in galaxies. Generally, DLAs, sub-DLAs (s-DLAs), Lyman limit systems (LLSs) and partial-LLSs (pLLSs) are used to study the evolution of metallicity of gas around the galaxies which show an increasing trend with age of the Universe (Rafelski et al. 2012; Lehner et al. 2013, 2016; Quiret et al. 2016; Wotta et al. 2019). In this section, we compare the redshift evolution of $[C/H]$ of C III absorbers with the redshift evolution of metallicity of DLAs, s-DLAs, and pLLS + LLS systems. As we have discussed before, the C III absorbers studied here are optically thin to Lyman continuum radiation and typically have $N(\text{H I}) < 10^{17} \text{ cm}^{-2}$.

In Fig. 9, we show the $[C/H]$ evolution of C III absorbers as a function of redshift (and time since big bang). At high- z , the scatter in metallicity is larger (over ≈ 3 dex spread in $[C/H]$) compared to the low- z (≈ 2 dex spread in $[C/H]$). As seen from panel (c) of Fig. 7, most of the systems with super-solar metallicity at high- z have $N(\text{H I}) < 10^{14} \text{ cm}^{-2}$. Such systems are not represented in the low- z sample due to the $N(\text{H I})$ cutoff used for the sample selection. When restricting to the same $N(\text{H I})$ range for low- z and high- z , we find the scatter at high- z is reduced considerably.

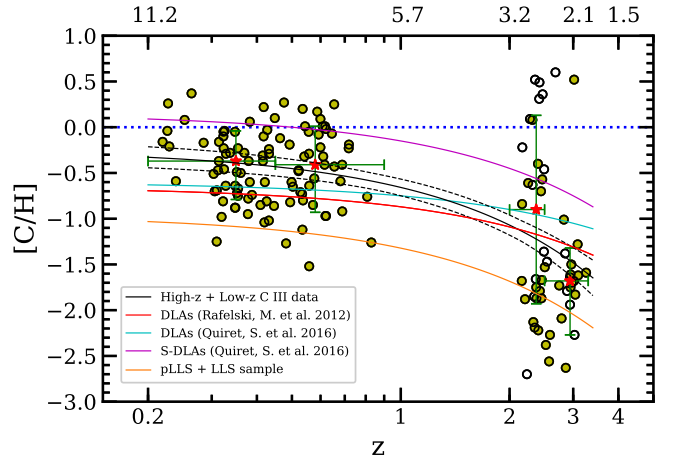


Figure 9. $[C/H]$ versus redshift (time since big bang). The scattered points show the combined C III systems whereas the yellow filled circles are C III systems with $N(\text{H I}) \geq 10^{15} \text{ cm}^{-2}$. The thick stars denote the median value of the $[C/H]$ obtained over the extent of the horizontal bar in the redshift range and the vertical bar denote 1σ range in shown median values. The black solid line denotes the linear regression fit (LRF) to $[C/H]$ vs. z and the black dotted lines indicate 1σ deviation around the LRF. The red, cyan, magenta and orange lines show the LRF fits from the measurements of cosmic metallicity of DLAs from Rafelski et al. (2012), Quiret et al. (2016), sub-DLAs from Quiret et al. (2016) and pLLSs + LLSs from Lehner et al. (2013, 2016); Wotta et al. (2019), respectively.

Fig. 9 suggests a strong evolution in metallicity between $z \approx 2.5$ and $z \approx 1.0$ (the age of the universe between ≈ 2.5 to 5.8 Gyr). The evolution becomes relatively slower in later times as seen from the median $[C/H]$ values in Fig. 9 (thick stars). We find a strong anti-correlation between z and $[C/H]$ with $\rho_s = -0.44$ at a significance level of 5.40σ . The LRF to $[C/H]$ vs. z gives a slope, -0.41 ± 0.05 with intercept, -0.25 ± 0.08 .

We compare the redshift evolution of $[C/H]$ of the C III absorbers with the cosmic metallicity (Z) evolution of DLAs (Rafelski et al. 2012; Quiret et al. 2016), sub-DLAs (Quiret et al. 2016) and pLLSs + LLSs (Lehner et al. 2013, 2016; Wotta et al. 2019). The redshift evolution of cosmic metallicity of DLAs measured by Rafelski et al. (2012) shows a shallower slope [$\langle Z \rangle = (-0.22 \pm 0.03)z - (0.65 \pm 0.09)$] upto $z \approx 5$ (denoted by red line in Fig. 9). Similarly, a LRF to $\langle Z \rangle$ vs. z for DLAs measured by Quiret et al. (2016) in the redshift, $0 < z < 4$ shows a slope of -0.15 ± 0.03 with a higher intercept, $-(0.6 \pm 0.13)$ (denoted by cyan line) whereas the LLSs in their data show a more elevated slope with redshift, $\langle Z \rangle = (-0.3 \pm 0.07)z - (0.15 \pm 0.31)$ (denoted by magenta line). The low- z ($z < 1$) and high- z ($2.3 < z < 3.4$) pLLSs + LLSs are selected from Lehner et al. (2013); Wotta et al. (2019) and Lehner et al. (2016), respectively. The LRF to the combined pLLSs + LLSs sample across redshift range, $0.2 < z < 3.4$ gives a slope, -0.36 ± 0.10 with an intercept, -0.95 ± 0.12 (denoted by orange line in Fig. 9). As seen from Fig. 9, the slope we measure for the combined low- z and high- z C III samples are higher than that measured for DLAs but consistent within the error range measured for sub-DLAs for high- $[C/H]$ branch and pLLSs + LLSs for low- $[C/H]$ branch of the C III absorbers.

5 SUMMARY

We have constructed a sample of C III absorption systems in optically thin H I clouds using the COS CGM compendium (CCC) sample of L18 at low- z i.e., in the range, $0.2 \leq z \leq 0.9$. We find a total of 99 C III absorption systems from the CCC sample with $N(\text{H I})$ (cm^{-2}) in the range, $15.0 \leq \log N(\text{H I}) \leq 16.2$. The observed $N(\text{H I})$, $N(\text{C II})$, $N(\text{C III})$ and column densities of other available metal ions along with their associated errors in the measured values have been adapted from the L18 measurements. We performed photoionization models for each of these individual C III systems using CLOUDY with the updated KS19 UVB ($\alpha = -1.8$) as the incident radiation field. We have discussed the implications of the observed and derived properties of the C III absorbers systematically. We have also combined the low- z systems with the high- z C III absorption systems from M19 to study the various correlation between the physical and chemical properties of the optically thin C III absorption systems. We have also shown the redshift evolution of the inferred properties of the C III absorbers for a wide redshift range from 0 – 3.3 in compliment with our PI models. Our main results are as follows:

- Under the single-phase PI models, the derived hydrogen density (n_{H}) of the low- z optically thin C III absorption systems ranges from $10^{-3.4}$ - $10^{-1.6} \text{ cm}^{-3}$ with a median value of $10^{-2.5} \text{ cm}^{-3}$. The median n_{H} of the low- z C III systems is 0.6 dex higher than the high- z systems analysed in M19. When we use four sub-samples divided in redshift bins, the redshift evolution of n_{H} is not monotonous.

- Metallicity, denoted as $[C/H]$, for the low- z absorbers show a unimodal distribution ranged from -1.6 to 0.4, with a median value of -0.46. The distribution of $[C/H]$ for the low and high redshift C III systems show a large spread which indicates that the absorbers are originating from the CGM of host galaxies having significantly different physical and chemical properties. We found a strong redshift evolution of $[C/H]$ between low- z and high- z absorbers. For the C III absorbers with $N(\text{H I})$ (cm^{-2}) $> 10^{15}$, we found that the low- z systems have $\approx 14\%$ absorbers with super solar metallicity and are more metal enriched than the high- z counterparts which have only $\approx 3\%$ super solar systems.

- The over-density of the low- z C III systems show a range from 3–4.5 with a median value of 3.74 which suggests that the absorbers are indeed originating from the high over-dense regions like CGM. The large difference in the median Δ between low- z and high- z C III absorbers (≈ 1.6 dex) is mainly due to the redshift evolution of the mean density, $\overline{n_{\text{H}}}$.

- The derived line-of-sight thickness (L) of the low- z C III systems are ranging from 1.3 pc to 10 kpc with a median value of 0.6 kpc which is ~ 10 times lower than the high- z counterparts. The difference in physical parameters (like n_{H} , $[C/H]$, Δ and L) of the absorbers suggest a strong redshift evolution of these quantities between low- z and high- z C III systems. The distribution of L is also significantly different between high- z and low- z C III systems. While there are significant numbers of sub-kpc size absorbers (78%) present at low- z , only 6% of the absorbers at high- z show such sub-kpc scale line-of-sight thickness. This clearly indicates that the low- z C III absorbers are metal enriched, dense and compact clouds compared to the high- z counterparts.

- We find a statistically significant anti-correlation between L vs. $[C/H]$ for the combined C III sample, which suggests that the highest metallicity systems are the tiniest in size. However, unlike high- z C III absorbers, the low- z absorbers are typically smaller in size for a given $[C/H]$ as predicted by the toy model used in

M19. This may be due to the slight enhancement in n_{H} at low- z and existence of moderate level (i.e., 2σ) correlation between n_{H} and $[C/H]$ in which case the clouds will have a shorter cooling time scale (or cooling length). Another possibility of the existence of such small scale absorbers could be the fragmentation of a larger high metallicity cloud where the parent cloud is fragmented to tiny cloudlets to reach pressure equilibrium with its surroundings efficiently at a final cooling time scale (McCourt et al. 2018).

- We see a clear segregation of the high $[C/H]$ and low $[C/H]$ branch absorbers occupied in distinct regions of L vs. $N(\text{C III})$ plane consistent with the two populations idea suggested by Kim et al. (2016). We find that the high- $[C/H]$ branch absorbers ($[C/H] > -1.2$) with $L < 0.25$ kpc show a strong correlation with $N(\text{C III})$, whereas, the low- $[C/H]$ branch absorbers do not exhibit such correlation with $N(\text{C III})$. However, the high- $[C/H]$ branch absorbers are mostly contributed by low- z systems and low- $[C/H]$ by high- z systems. Hence, an increased number of C III absorbers spanning in the L vs. $N(\text{C III})$ plane uniformly is required to confirm the existence of a statistically significant bimodality in metallicity. The results will have implications in understanding the metal enrichment of the CGM gas and its evolution.

- Finally, we compare the redshift evolution of $[C/H]$ with the different class of absorption systems (DLAs, s-DLAs, pLLSs and LLSs). As seen in Fig. 9, the metallicity of the C III absorbers show a strong evolution between $z \approx 2.5$ and $z \approx 1$ while the age of the Universe was between ≈ 2.5 Gyr to 5.8 Gyr. The evolution is relatively slower at a later stage of the Universe. The linear regression fit to the z vs. $[C/H]$ gives a slope -0.41 ± 0.05 with intercept, -0.25 ± 0.08 . This is steeper than that measured for DLAs (Rafelski et al. 2012; Quiret et al. 2016). Interestingly, the elevated slope of the C III absorbers are within the error range of the measured slope of s-DLAs from Quiret et al. (2016) and pLLSs + LLSs sample across redshift from Lehner et al. (2013, 2016); Wotta et al. (2019). However, we reiterate the fact that our results may be illusive owing to the lack of the low- n_{H} absorbers at low- z as well as lack of C III absorbers in the intermediate redshift ($0.9 \leq z \leq 2.1$).

To make further progress in this field, it will be important to search for such C III absorbers in the intermediate redshift ranges (i.e., $1.0 \leq z \leq 2.0$) and at higher redshift (i.e., $z > 3$) with uniform coverage in $N(\text{H I})$. This will allow to create a homogeneous C III sample across a large redshift ranges.

ACKNOWLEDGMENTS

The authors wish to thank the anonymous referee for providing valuable comments and suggestions for improving the manuscript. AM acknowledges the Department of Science and Technology (DST), Government of India for financial support through DST-INSPIRE fellowship (IF150845). AM and ACP wish to thank the Inter-University Centre for Astronomy and Astrophysics (IUCAA), India for providing hospitality and travel grants.

DATA AVAILABILITY

The data underlying this article are available in Vizier On-line Data Catalog: J/ApJ/866/33, at <https://cdsarc.unistra.fr/viz-bin/cat/J/ApJ/866/33>.

References

- Adelberger K. L., Shapley A. E., Steidel C. C., Pettini M., Erb D. K., Reddy N. A., 2005, *ApJ*, **629**, 636
- Bergeron J., 1986, *A&A*, **155**, L8
- Bergeron J., Herbert-Fort S., 2005, in Williams P., Shu C.-G., Menard B., eds, IAU Colloq. 199: Probing Galaxies through Quasar Absorption Lines. pp 265–280, doi:10.1017/S1743921305002693
- Boksenberg A., Sargent W. L. W., 2015, *ApJS*, **218**, 7
- Bouma S. J. D., Richter P., Fechner C., 2019, *A&A*, **627**, A20
- Chen H.-W., Lanzetta K. M., Webb J. K., 2001, *ApJ*, **556**, 158
- Chen H.-W., Helsby J. E., Gauthier J.-R., Shectman S. A., Thompson I. B., Tinker J. L., 2010, *ApJ*, **714**, 1521
- Cowie L. L., Songaila A., Kim T.-S., Hu E. M., 1995, *AJ*, **109**, 1522
- Dedikov S. Y., Shechkinov Y. A., 2004, *Astronomy Reports*, **48**, 9
- Dutta R., Srianand R., Gupta N., Joshi R., 2017, *MNRAS*, **468**, 1029
- Feigelson E. D., Nelson P. I., 1985, *ApJ*, **293**, 192
- Ferland G. J., et al., 2013, *Rev. Mexicana Astron. Astrofis.*, **49**, 137
- Ferland G. J., et al., 2017, *Rev. Mexicana Astron. Astrofis.*, **53**, 385
- Field G. B., 1965, *ApJ*, **142**, 531
- Ford A. B., Davé R., Oppenheimer B. D., Katz N., Kollmeier J. A., Thompson R., Weinberg D. H., 2014, *MNRAS*, **444**, 1260
- Fox A., Davé R., 2017, *Gas Accretion onto Galaxies*. Vol. 430, doi:10.1007/978-3-319-52512-9
- Gaikwad P., Khaire V., Choudhury T. R., Srianand R., 2017a, *MNRAS*, **466**, 838
- Gaikwad P., Srianand R., Choudhury T. R., Khaire V., 2017b, *MNRAS*, **467**, 3172
- Gaikwad P., Choudhury T. R., Srianand R., Khaire V., 2018, *MNRAS*, **474**, 2233
- Gaikwad P., Srianand R., Khaire V., Choudhury T. R., 2019, *MNRAS*, **490**, 1588
- Grevesse N., Asplund M., Sauval A. J., Scott P., 2010, *Ap&SS*, **328**, 179
- Haardt F., Madau P., 2012, *ApJ*, **746**, 125
- Hafen Z., et al., 2020, *MNRAS*, **494**, 3581
- Heckman T. M., Lehnert M. D., Strickland D. K., Armus L., 2000, *ApJS*, **129**, 493
- Heckman T., Borthakur S., Wild V., Schiminovich D., Bordoloi R., 2017, *ApJ*, **846**, 151
- Herenz P., Richter P., Charlton J. C., Masiero J. R., 2013, *A&A*, **550**, A87
- Ho S. H., Martin C. L., 2020, *ApJ*, **888**, 14
- Hussain T., Khaire V., Srianand R., Muzahid S., Pathak A., 2017, *MNRAS*, **466**, 3133
- Inoue A. K., Shimizu I., Iwata I., Tanaka M., 2014, *MNRAS*, **442**, 1805
- Isobe T., Feigelson E. D., Nelson P. I., 1986, *ApJ*, **306**, 490
- Joshi R., Srianand R., Petitjean P., Noterdaeme P., 2017, *MNRAS*, **471**, 1910
- Keeney B. A., et al., 2017, *ApJS*, **230**, 6
- Khaire V., 2017, *MNRAS*, **471**, 255
- Khaire V., Srianand R., 2015a, *MNRAS*, **451**, L30
- Khaire V., Srianand R., 2015b, *ApJ*, **805**, 33
- Khaire V., Srianand R., 2019, *MNRAS*, **484**, 4174
- Kim T.-S., Carswell R. F., Ranquist D., 2016, *MNRAS*, **456**, 3509
- Kollmeier J. A., et al., 2014, *ApJ*, **789**, L32
- Lavalley M., Isobe T., Feigelson E., 1992, in Worrall D. M., Biemesderfer C., Barnes J., eds, *Astronomical Society of the Pacific Conference Series* Vol. 25, *Astronomical Data Analysis Software and Systems I*. p. 245
- Lehner N., et al., 2013, *ApJ*, **770**, 138
- Lehner N., O’Meara J. M., Howk J. C., Prochaska J. X., Fumagalli M., 2016, *ApJ*, **833**, 283
- Lehner N., Wotta C. B., Howk J. C., O’Meara J. M., Oppenheimer B. D., Cooksey K. L., 2018, *ApJ*, **866**, 33
- Lehner N., Wotta C. B., Howk J. C., O’Meara J. M., Oppenheimer B. D., Cooksey K. L., 2019, *ApJ*, **887**, 5
- Liang C. J., Remming I., 2020, *MNRAS*, **491**, 5056
- Lochhaas C., Thompson T. A., Quataert E., Weinberg D. H., 2018, *MNRAS*, **481**, 1873
- Lusso E., Worsack G., Hennawi J. F., Prochaska J. X., Vignali C., Stern J., O’Meara J. M., 2015, *MNRAS*, **449**, 4204
- McCourt M., O’Leary R. M., Madigan A.-M., Quataert E., 2015, *MNRAS*, **449**, 2
- McCourt M., Oh S. P., O’Leary R., Madigan A.-M., 2018, *MNRAS*, **473**, 5407
- Mohapatra A., Srianand R., Khaire V., Pradhan A. C., 2019, *MNRAS*, **484**, 5028
- Muratov A. L., Kereš D., Faucher-Giguère C.-A., Hopkins P. F., Quataert E., Murray N., 2015, *MNRAS*, **454**, 2691
- Muzahid S., 2014, *ApJ*, **784**, 5
- Muzahid S., Kacprzak G. G., Churchill C. W., Charlton J. C., Nielsen N. M., Mathes N. L., Trujillo-Gomez S., 2015, *ApJ*, **811**, 132
- Muzahid S., Fonseca G., Roberts A., Rosenwasser B., Richter P., Narayanan A., Churchill C., Charlton J., 2018, *MNRAS*, **476**, 4965
- Narayanan A., Charlton J. C., Masiero J. R., Lynch R., 2005, *ApJ*, **632**, 92
- Petitjean P., Bergeron J., 1990, *A&A*, **231**, 309
- Prochaska J. X., et al., 2017, *ApJ*, **837**, 169
- Qiret S., et al., 2016, *MNRAS*, **458**, 4074
- Rafelski M., Wolfe A. M., Prochaska J. X., Neeleman M., Mendez A. J., 2012, *ApJ*, **755**, 89
- Schaye J., 2001, *ApJ*, **559**, 507
- Schaye J., Carswell R. F., Kim T.-S., 2007, *MNRAS*, **379**, 1169
- Scott J. E., Kriss G. A., Brotherton M., Green R. F., Hutchings J., Shull J. M., Zheng W., 2004, *ApJ*, **615**, 135
- Shull J. M., Stevans M., Danforth C. W., 2012, *ApJ*, **752**, 162
- Shull J. M., Moloney J., Danforth C. W., Tilton E. M., 2015, *ApJ*, **811**, 3
- Steidel C. C., Erb D. K., Shapley A. E., Pettini M., Reddy N., Bogosavljević M., Rudie G. C., Rakic O., 2010, *ApJ*, **717**, 289
- Stern J., Hennawi J. F., Prochaska J. X., Werk J. K., 2016, *ApJ*, **830**, 87
- Stevans M. L., Shull J. M., Danforth C. W., Tilton E. M., 2014, *ApJ*, **794**, 75
- Stocke J. T., Keeney B. A., Danforth C. W., Shull J. M., Froning C. S., Green J. C., Penton S. V., Savage B. D., 2013, *ApJ*, **763**, 148
- Telfer R. C., Zheng W., Kriss G. A., Davidsen A. F., 2002, *ApJ*, **565**, 773
- Thompson T. A., Quataert E., Zhang D., Weinberg D. H., 2016, *MNRAS*, **455**, 1830
- Tilton E. M., Stevans M. L., Shull J. M., Danforth C. W., 2016, *ApJ*, **817**, 56
- Tumlinson J., Peebles M. S., Werk J. K., 2017, *ARA&A*, **55**, 389
- Vanden Berk D. E., et al., 2001, *AJ*, **122**, 549
- Veilleux S., Cecil G., Bland-Hawthorn J., 2005, *ARA&A*, **43**, 769
- Werk J. K., Prochaska J. X., Thom C., Tumlinson J., Tripp T. M., O’Meara J. M., Peebles M. S., 2013, *ApJS*, **204**, 17
- Werk J. K., et al., 2014, *ApJ*, **792**, 8
- Wotta C. B., Lehner N., Howk J. C., O’Meara J. M., Oppenheimer B. D., Cooksey K. L., 2019, *ApJ*, **872**, 81
- Zhang D., 2018, *Galaxies*, **6**, 114

APPENDIX A: CORRELATIONS AMONG VARIOUS MODEL PREDICTED PARAMETERS OF THE LOW- Z C III SAMPLE

In this appendix, we show the correlation between derived parameters of the low- z absorbers that are discussed in §4.2 (indicated by circles in Fig. 7). In panel (a) of Fig. A1, we present the anti-correlation between L and $[C/H]$. The symbols are colour coded with $\log n_{\text{H}}$ values as shown in the side colour bar. We show the correlation between L vs. $N(\text{C III})$ and L vs. $N(\text{H I})$ in panel (b) and panel (c) of Fig. A1, respectively. In addition to the colour coding of n_{H} as used in panel (a), we colour code $[C/H]$ values (thick rings) as shown in the side colour bars of these panels. In panel (d) and panel (e) of Fig. A1, we plot the correlation between $[C/H]$ vs. $N(\text{C III})$ and $[C/H]$ vs. $N(\text{H I})$, respectively. The symbol sizes increase with the increasing of redshifts for the figures in all panels. The correlation coefficient with significance level as indicated in the legends of each panels of Fig. A1 are discussed in §4.2.

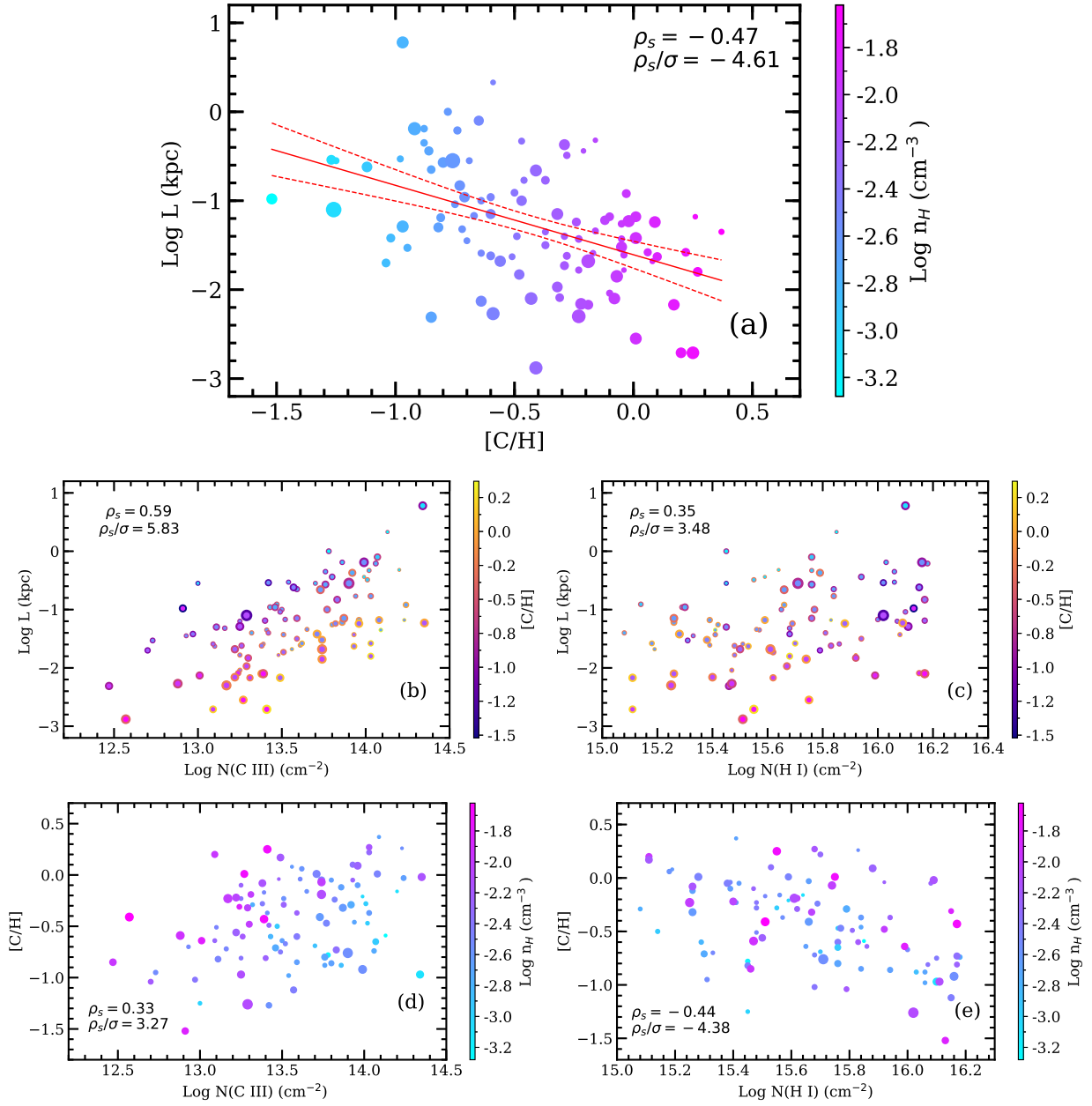


Figure A1. The plots show correlations among various model predicted parameters of the low- z C III sample. We show the Spearman rank correlation coefficients (ρ_s) and significance levels (ρ_s/σ) in the legends. Panel (a): L vs. $[C/H]$ and the symbols are colour coded with $\log n_{\text{H}}$ values as shown in the side colour bar. The solid line shows the LRF to the data and the dashed solid lines indicate the 1σ deviation around the LRF. Middle panels: L vs. $N(\text{C III})$ (panel (b)) and L vs. $N(\text{H I})$ (panel (c)) with additional colour codings of $[C/H]$ values (thick rings) as shown in the side colour bars. Bottom panels: $[C/H]$ vs. $N(\text{C III})$ (panel (d)) and $[C/H]$ vs. $N(\text{H I})$ (panel (e)) with the same colour coding of n_{H} as used in the top panel. The symbol sizes increase with the increasing of redshifts for all the figures.

APPENDIX B: DETAILS OF THE LOW- Z SAMPLE AND PHOTOIONIZATION (PI) MODEL OUTPUTS

In this appendix, we provide the details of the low- z absorbers which are analysed in this work along with the results of PI models. In Table B1, we give the details of the observed column densities of C III and C II ions along with the flags in the measurements. We also provide the results of PI models for each on these absorbers. In Table B2 and B3, we provide the details of the absorbers for which

there are associations of other metal ion combinations (i.e., sample SA2 of the low- z absorbers).

Table B1: Summary of low- z C III sample and photoionization (PI) model predicted parameters.

IDs	z_{abs}	Observed					PI model						
		$\log N(\text{H I})$ (cm^{-2})	$\log N(\text{C III})$ (cm^{-2})	Flag	$\log N(\text{C II})$ (cm^{-2})	Flag	Flag on $\frac{N(\text{C III})}{N(\text{C II})}$	$\log n_{\text{H}}$ (cm^{-3})	$[\text{C}/\text{H}]$	$\log L$ (kpc)	$\log \Delta$	$\log N(\text{C III})$ (cm^{-2})	$\log N(\text{C II})$ (cm^{-2})
(1)	(2)	(3)	(4)	(5)	(6)	(7)	(8)	(9)	(10)	(11)	(12)	(13)	(14)
1	0.21945	15.64 ± 0.04	> 14.20	-2	< 13.57	-1	-2*	-3.09	-0.16	-0.32	3.42	14.25	13.42
2	0.22620	15.92 ± 0.09	13.48 ± 0.09	0	< 13.62	-1	-2	-2.25	-0.04	-1.78	4.25	13.53	13.58
3	0.22719	15.83 ± 0.01	> 14.23	-2	13.84 ± 0.08	0	-2*	-2.56	+0.26	-1.18	3.92	14.24	13.93
4	0.22902	15.59 ± 0.04	> 13.99	-2	< 13.59	-1	-2*	-3.05	-0.21	-0.44	3.45	14.13	13.32
5	0.23881	15.85 ± 0.03	> 14.13	-2	< 13.39	-1	-2*	-3.28	-0.59	+0.33	3.21	14.26	13.18
6	0.25247	15.19 ± 0.01	13.56 ± 0.01	0	< 13.04	-1	-2*	-2.63	+0.08	-1.68	3.84	13.54	13.14
7	0.26382	15.41 ± 0.02	> 14.09	-2	< 13.67	-1	-2*	-2.68	+0.37	-1.35	3.78	14.12	13.66
8	0.28495	15.51 ± 0.06	13.39 ± 0.06	0	< 13.29	-1	-2*	-2.50	-0.17	-1.59	3.94	13.49	13.18
9	0.30371	15.48 ± 0.06	13.1 ± 0.06	0	< 13.08	-1	-2	-2.48	-0.51	-1.63	3.94	13.13	12.81
10	0.30579	15.33 ± 0.06	12.93 ± 0.06	0	< 12.83	-1	-2	-2.51	-0.70	-1.45	3.79	13.01	12.51
11	0.30963	15.45 ± 0.12	13.00 ± 0.12	0	< 12.97	-1	-2	-3.00	-1.25	-0.55	3.41	13.02	12.13
12	0.30995	15.70 ± 0.05	> 13.70	-2	< 13.03	-1	-2	-2.88	-0.69	-0.55	3.53	13.70	12.93
13	0.31230	15.76 ± 0.05	14.02 ± 0.05	0	< 13.24	-1	-2	-2.96	-0.47	-0.33	3.45	14.07	13.22
14	0.31387	15.57 ± 0.06	13.41 ± 0.06	0	< 13.23	-1	-2	-2.56	-0.37	-1.35	3.85	13.49	13.07
15	0.31426	15.56 ± 0.04	13.65 ± 0.04	0	< 13.32	-1	-2	-2.57	-0.16	-1.34	3.84	13.71	13.27
16	0.31950	16.06 ± 0.03	13.54 ± 0.03	0	< 13.02	-1	-2	-2.71	-0.98	-0.53	3.69	13.59	12.99
17	0.32246	16.07 ± 0.04	13.25 ± 0.04	0	< 13.30	-1	-2	-2.38	-0.81	-1.20	4.02	13.33	13.08
18	0.32307	15.47 ± 0.02	13.25 ± 0.02	0	13.17 ± 0.09	0	0	-2.27	-0.10	-2.04	4.13	13.27	13.14
19	0.32340	16.08 ± 0.01	13.93 ± 0.01	0	13.81 ± 0.02	0	0	-2.27	-0.05	-1.43	4.13	13.94	13.80
20	0.32377	15.48 ± 0.10	13.25 ± 0.1	0	< 13.22	-1	-2	-2.39	-0.23	-1.78	4.01	13.33	13.07
21	0.32451	15.84 ± 0.01	> 13.94	-2	< 13.22	-1	-2*	-2.70	-0.46	-0.77	3.70	13.91	13.28
22	0.32565	15.39 ± 0.01	13.61 ± 0.01	0	13.21 ± 0.04	0	0*	-2.51	-0.04	-1.61	3.89	13.61	13.21
23	0.32793	15.86 ± 0.08	13.09 ± 0.08	0	< 13.22	-1	-2	-2.29	-0.64	-1.59	4.11	13.18	13.01
24	0.32848	15.08 ± 0.04	13.32 ± 0.04	0	< 13.66	-1	-2	-2.76	-0.29	-1.40	3.63	13.37	12.70
25	0.33719	15.55 ± 0.04	> 14.01	-2	< 13.59	-1	-2*	-2.96	-0.28	-0.49	3.43	14.09	13.19
26	0.34793	16.06 ± 0.01	13.76 ± 0.01	0	< 13.40	-1	-2*	-2.70	-0.88	-0.35	3.61	13.82	13.10
27	0.34800	15.42 ± 0.04	13.8 ± 0.04	0	< 13.42	-1	-2	-2.65	-0.05	-1.26	3.73	13.85	13.27
28	0.34833	15.65 ± 0.02	13.5 ± 0.02	0	< 13.03	-1	-2	-2.66	-0.64	-1.00	3.72	13.51	12.91
29	0.34873	16.03 ± 0.01	> 13.86	-2	< 13.08	-1	-2*	-2.86	-0.88	-0.19	3.51	13.89	13.08
30	0.35197	15.81 ± 0.06	13.42 ± 0.06	0	13.26 ± 0.19	0	0	-2.32	-0.49	-1.40	3.98	13.47	13.15
31	0.35231	15.68 ± 0.09	13.16 ± 0.09	0	< 13.10	-1	-2	-2.49	-0.72	-1.32	3.88	13.24	12.82
32	0.35460	16.10 ± 0.12	> 13.49	-2	< 13.24	-1	-2	-2.42	-0.75	-1.04	3.95	13.54	13.20
33	0.35471	15.41 ± 0.14	13.51 ± 0.14	0	< 13.31	-1	-2*	-2.57	-0.23	-1.43	3.80	13.56	13.06
34	0.35493	16.00 ± 0.09	> 13.52	-2	< 13.18	-1	-2	-2.49	-0.67	-1.17	3.96	13.51	13.17
35	0.36074	15.14 ± 0.01	13.47 ± 0.01	0	12.56 ± 0.06	0	0*	-2.94	-0.50	-0.91	3.42	13.47	12.56
36	0.36921	15.48 ± 0.06	13.38 ± 0.06	0	< 13.04	-1	-2	-2.43	-0.28	-1.62	3.93	13.43	13.05
37	0.37771	15.31 ± 0.09	12.73 ± 0.09	0	< 12.71	-1	-2*	-2.53	-0.95	-1.53	3.82	12.78	12.25
38	0.37845	15.45 ± 0.02	13.78 ± 0.02	0	< 12.85	-1	-2*	-3.19	-0.78	+0.00	3.16	13.80	12.56
39	0.37954	15.94 ± 0.05	13.59 ± 0.05	0	13.37 ± 0.10	0	0	-2.26	-0.37	-1.50	4.09	13.59	13.37
40	0.38233	15.29 ± 0.04	13.43 ± 0.04	0	< 12.82	-1	-2	-2.81	-0.60	-0.96	3.53	13.45	12.62
41	0.38243	15.18 ± 0.08	13.62 ± 0.08	0	< 13.12	-1	-2	-2.59	+0.06	-1.58	3.75	13.69	13.13
42	0.38759	16.18 ± 0.02	> 14.06	-2	< 13.39	-1	-2*	-2.73	-0.74	-0.21	3.61	14.15	13.37
43	0.40936	15.84 ± 0.04	13.59 ± 0.04	0	< 13.87	-1	-2*	-2.66	-0.85	-0.65	3.66	13.67	12.92
44	0.41510	16.15 ± 0.13	13.24 ± 0.13	0	< 13.48	-1	-2	-1.85	-0.31	-2.09	4.46	13.29	13.46
45	0.41565	15.84 ± 0.01	> 14.03	-2	< 13.38	-1	-2*	-2.63	-0.37	-0.77	3.68	14.05	13.38
46	0.41747	15.39 ± 0.01	13.96 ± 0.01	0	< 13.16	-1	-2*	-2.65	-0.10	-1.18	3.66	13.93	13.19
47	0.41774	15.70 ± 0.01	> 14.03	-2	13.75 ± 0.05	0	-2	-2.31	+0.22	-1.58	4.00	14.08	13.75
48	0.41969	15.79 ± 0.12	12.7 ± 0.12	0	< 13.04	-1	-2	-2.21	-1.04	-1.70	4.10	12.77	12.55
49	0.42079	15.83 ± 0.03	13.26 ± 0.03	0	< 13.08	-1	-2	-2.21	-0.60	-1.62	4.10	13.30	13.05
50	0.42559	16.17 ± 0.11	13.40 ± 0.11	0	< 13.40	-1	-2*	-2.26	-0.81	-1.19	4.04	13.49	13.19
51	0.42731	15.66 ± 0.03	> 14.24	-2	< 13.55	-1	-2*	-2.66	-0.03	-0.92	3.64	14.21	13.52
52	0.43177	15.68 ± 0.04	12.97 ± 0.04	0	< 12.62	-1	-2	-2.39	-1.02	-1.42	3.91	12.95	12.52
53	0.43196	15.69 ± 0.03	> 13.82	-2	< 13.35	-1	-2*	-2.47	-0.24	-1.24	3.83	13.84	13.33
54	0.43221	15.62 ± 0.09	13.51 ± 0.09	0	< 13.13	-1	-2	-2.27	-0.29	-1.73	4.03	13.46	13.15
55	0.44609	15.94 ± 0.01	> 13.80	-2	< 13.05	-1	-2*	-2.67	-0.86	-0.44	3.61	13.85	13.03
56	0.44837	15.53 ± 0.05	13.93 ± 0.05	0	13.36 ± 0.15	0	0	-2.35	+0.10	-1.63	3.93	13.90	13.48
57	0.46370	15.26 ± 0.02	13.86 ± 0.02	0	< 12.96	-1	-2	-2.67	-0.12	-1.22	3.60	13.82	13.05
58	0.47547	15.68 ± 0.08	> 14.03	-2	13.69 ± 0.16	0	-2	-2.18	+0.27	-1.80	4.08	14.03	13.76
59	0.48168	16.02 ± 0.10	13.42 ± 0.1	0	< 12.74	-1	-2*	-2.57	-1.27	-0.54	3.68	13.45	12.69
60	0.49263	15.62 ± 0.06	13.31 ± 0.06	0	< 13.13	-1	-2	-2.02	-0.19	-2.17	4.22	13.30	13.18
61	0.49450	15.45 ± 0.02	13.11 ± 0.02	0	< 12.87	-1	-2*	-2.48	-0.82	-1.30	3.76	13.22	12.55
62	0.49888	15.76 ± 0.06	13.59 ± 0.06	0	< 13.29	-1	-2*	-2.42	-0.60	-1.15	3.82	13.64	13.05
63	0.50297	15.76 ± 0.08	> 14.07	-2	< 13.09	-1	-2	-2.94	-0.65	-0.10	3.29	14.12	13.01
64	0.52147	15.92 ± 0.05	13.30 ± 0.05	0	< 13.79	-1	-2	-2.02	-0.48	-1.83	4.20	13.37	13.21
65	0.52208	15.77 ± 0.06	13.77 ± 0.06	0	< 13.36	-1	-2	-2.49	-0.47	-1.00	3.73	13.85	13.19
66	0.52794	15.30 ± 0.01	13.46 ± 0.01	0	12.52 ± 0.19	0	0	-2.73	-0.71	-0.96	3.48	13.42	12.50
67	0.53351	16.17 ± 0.10	> 13.83	-2	< 13.63	-1	-2*	-2.35	-0.73	-0.83	3.86	13.90	13.34
68	0.53459	16.15 ± 0.11	13.57 ± 0.11	0	< 13.52 ± 0.16	-1	-2*	-2.44	-1.12	-0.62	3.77	13.64	12.96
69	0.53538	15.11 ± 0.06	13.09 ± 0.06	0	< 13.07	-1	-2	-1.98	+0.20	-2.71	4.23	13.20	13.06
70	0.53649	15.76 ± 0.02	13.76 ± 0.02	0	< 13.07	-1	-2	-2.69	-0.80	-0.57	3.52	13.77	12.87
71	0.54105	15.67 ± 0.09	13.29 ± 0.09	0	< 13.34	-1	-2	-2.06	-0.32	-1.97	4.14	13.37	13.14
72	0.54368	15.59 ± 0.02	> 14.08	-2	< 13.67	-1	-2	-2.48	+0.01	-1.18	3.72	14.17	13.49
73	0.55647	15.38 ± 0.06	> 13.74	-2	< 13.35	-1	-2*	-2.45	-0.05	-1.52	3.74	13.79	13.19
74	0.55753	15.79 ± 0.04	> 13.92	-2	13.44 ± 0.10	0	-2*	-2.74	-0.29	-0.37	3.45	14.34	13.42

Table B1 (continued)

Table B1 (continued)

IDs	z_{abs}	Observed					PI model						
		$\log N(\text{H I})$ (cm^{-2})	$\log N(\text{C III})$ (cm^{-2})	Flag	$\log N(\text{C II})$ (cm^{-2})	Flag	Flag on $\frac{N(\text{C III})}{N(\text{C II})}$	$\log n_{\text{H}}$ (cm^{-3})	$[\text{C}/\text{H}]$	$\log L$ (kpc)	$\log \Delta$	$\log N(\text{C III})$ (cm^{-2})	$\log N(\text{C II})$ (cm^{-2})
(1)	(2)	(3)	(4)	(5)	(6)	(7)	(8)	(9)	(10)	(11)	(12)	(13)	(14)
75	0.55820	16.13 ± 0.09	12.91 ± 0.09	0	< 13.43	-1	-2	-1.85	-1.52	-0.98	3.89	12.99	12.48
76	0.55845	15.99 ± 0.07	13.01 ± 0.07	0	13.13 ± 0.13	0	0	-1.82	-0.64	-2.13	4.37	13.04	13.04
77	0.57183	15.46 ± 0.16	12.47 ± 0.16	0	< 12.57	-1	-2	-1.98	-0.85	-2.31	4.20	12.56	12.38
78	0.57649	15.50 ± 0.06	13.22 ± 0.06	0	< 13.08	-1	-2*	-2.25	-0.56	-1.68	3.92	13.30	12.81
79	0.58756	15.11 ± 0.08	13.49 ± 0.08	0	< 13.5	-1	-2	-2.21	+0.17	-2.17	3.95	13.57	13.13
80	0.59276	15.26 ± 0.08	13.38 ± 0.08	0	< 12.98	-1	-2	-2.17	-0.08	-2.10	3.99	13.42	13.02
81	0.59954	15.40 ± 0.11	13.22 ± 0.11	0	< 13.35	-1	-2	-2.07	-0.22	-2.16	4.08	13.30	12.99
82	0.59956	15.88 ± 0.01	> 13.96	-2	13.85 ± 0.02	0	-2*	-2.27	+0.09	-1.24	3.88	14.29	13.84
83	0.60827	15.75 ± 0.14	13.27 ± 0.14	0	< 13.83	-1	-2	-1.71	+0.01	-2.55	4.44	13.35	13.41
84	0.61025	15.26 ± 0.04	> 13.87	-2	< 12.80	-1	-2*	-2.62	-0.32	-1.15	3.52	13.81	12.84
85	0.61566	15.66 ± 0.04	> 13.73	-2	13.16 ± 0.09	0	-2*	-2.63	-0.41	-0.66	3.51	14.12	13.16
86	0.61751	15.28 ± 0.04	> 13.71	-2	13.22 ± 0.06	0	-2	-2.47	+0.01	-1.42	3.67	13.84	13.19
87	0.61913	16.10 ± 0.04	> 14.34	-2	< 12.96	-1	-2*	-3.09	-0.97	+0.78	3.05	14.42	12.95
88	0.62138	16.11 ± 0.14	13.25 ± 0.14	0	< 13.16	-1	-2	-2.13	-0.97	-1.29	4.01	13.38	12.98
89	0.62143	16.09 ± 0.01	> 14.35	-2	13.90 ± 0.02	0	-2	-2.17	-0.02	-1.23	3.97	14.36	13.92
90	0.64492	15.74 ± 0.16	13.74 ± 0.16	0	< 13.61	-1	-2	-2.03	-0.07	-1.85	4.09	13.80	13.48
91	0.65440	15.55 ± 0.06	13.41 ± 0.06	0	< 13.51	-1	-2	-1.71	+0.25	-2.71	4.40	13.45	13.47
92	0.65506	16.17 ± 0.06	13.39 ± 0.06	0	< 13.46	-1	-2	-1.69	-0.43	-2.10	4.42	13.40	13.42
93	0.68121	15.47 ± 0.08	12.88 ± 0.08	0	< 12.67	-1	-2	-1.94	-0.59	-2.27	4.15	12.94	12.67
94	0.68857	15.51 ± 0.13	12.57 ± 0.13	0	< 12.90	-1	-2	-1.62	-0.41	-2.88	4.46	12.68	12.75
95	0.68895	16.16 ± 0.02	> 13.99	-2	< 13.54	-1	-2*	-2.56	-0.92	-0.19	3.52	14.11	13.17
96	0.71796	15.25 ± 0.10	13.17 ± 0.10	0	< 12.93	-1	-2	-2.01	-0.23	-2.30	4.05	13.23	12.84
97	0.71896	15.61 ± 0.11	> 13.74	-2	13.27 ± 0.10	0	-2*	-2.12	-0.19	-1.68	3.94	13.81	13.29
98	0.80775	15.71 ± 0.04	> 13.90	-2	< 12.94	-1	-2*	-2.55	-0.76	-0.55	3.44	13.96	12.86
99	0.82917	16.02 ± 0.05	13.29 ± 0.05	0	< 12.70	-1	-2*	-2.11	-1.26	-1.10	3.87	13.35	12.68

Note- Col ID (5): Flag on the column density measurement of C III. Col ID (7): Flag on the column density measurement of C II. Flag '0' represents detections whereas '-2' and '-1' indicate lower limits and upper limits, respectively. Col ID (8): Flag on observed $N(\text{C III})/N(\text{C II})$. Flag '0' indicates well constrained observed $N(\text{C III})/N(\text{C II})$ (sample SA1), '-2*' indicates lower limits on observed $N(\text{C III})/N(\text{C II})$ with other metal ions associations (sample SA2) and '-2' indicates lower limits on observed $N(\text{C III})/N(\text{C II})$ without presence of other metal ion combinations (sample SB).

Table B2. Summary of C III + Si III selected absorbers in sub-sample SA2 and PI model predicted parameters.

IDs	z_{abs}	Observed			PI model			
		$\log N(\text{Si III})$ (cm^{-2})	Flag	$\log N(\text{Si II})$ (cm^{-2})	Flag	$[\text{Si}/\text{H}]$	$\log N(\text{Si III})$ (cm^{-2})	$\log N(\text{Si II})$ (cm^{-2})
(1)	(2)	(3)	(4)	(5)	(6)	(7)	(8)	(9)
1	0.21945	12.99 ± 0.06	0	< 12.55	-1	-0.30	12.99	12.4
3	0.22719	12.84 ± 0.05	0	13.05 ± 0.04	0	+0.10	12.91	13.08
4	0.22902	12.84 ± 0.14	0	< 12.60	-1	-0.29	12.93	12.37
5	0.23881	12.85 ± 0.04	0	< 12.10	-1	-0.75	12.87	12.00
6	0.25247	12.16 ± 0.09	0	< 12.03	-1	-0.24	12.10	12.09
7	0.26382	12.99 ± 0.09	0	< 12.84	-1	+0.27	12.9	12.85
8	0.28495	12.73 ± 0.11	0	< 12.79	-1	+0.14	12.63	12.79
21	0.32451	12.99 ± 0.11	0	< 12.91	-1	-0.30	12.95	12.69
22 [@]	0.32565	12.58 ± 0.06	0	12.57 ± 0.17	0	+0.03	12.55	12.57
25	0.33719	13.47 ± 0.17	-2	< 12.76	-1	+0.16	13.39	12.75
26	0.34793	12.91 ± 0.05	0	12.48 ± 0.12	-1	-0.75	12.85	12.43
28	0.34833	12.55 ± 0.05	0	< 12.14	-1	-0.62	12.54	12.17
29	0.34873	12.89 ± 0.02	0	< 12.18	-1	-0.95	12.81	12.17
33	0.35471	12.95 ± 0.17	0	< 12.60	-1	+0.09	12.89	12.66
35 [@]	0.36074	12.65 ± 0.02	0	< 11.84	-1	-0.31	12.58	11.85
38*	0.37845	13.22 ± 0.02	0	< 12.02	-1	-0.17	13.16	12.02
45	0.41565	13.18 ± 0.09	0	< 12.70	-1	-0.26	13.09	12.72
46	0.41747	12.68 ± 0.06	0	< 12.51	-1	-0.25	12.64	12.27
49*	0.42079	12.31 ± 0.09	0	< 12.59	-1	-0.47	12.34	12.42
50	0.42559	13.15 ± 0.20	-2	< 13.19	-1	-0.22	12.91	13.08
51*	0.42731	13.29 ± 0.22	-2	< 13.19	-1	+0.19	13.28	13.07
53	0.43196	13.00 ± 0.14	-2	< 12.85	-1	-0.07	12.91	12.78
55*	0.44609	12.74 ± 0.05	0	< 12.41	-1	-0.87	12.8	11.99
57	0.46370	12.67 ± 0.11	0	< 12.74	-1	-0.12	12.71	12.25

Note:- 1. Col ID: (4) Flag in the column density measurement of Si III (6) Flag in the column density measurement of Si II. Flag '0' indicate detections whereas '-2' and '-1' indicate lower limits and upper limits, respectively.

2. The absorbers with IDs, 22 and 35 marked by '@' are included in SA1 as they have clean detection of C III + C II.

3. The absorbers marked with '*' have both Si III and O III detections. The same IDs are also marked in Table B3.

Table B3. Summary of C III + O III selected absorbers in sub-sample SA2 and PI model predicted parameters.

IDs	z_{abs}	Observed			PI model			
		$\log N(\text{O III})$ (cm^{-2})	Flag	$\log N(\text{O II})$ (cm^{-2})	Flag	$[\text{O}/\text{H}]$	$\log N(\text{O III})$ (cm^{-2})	$\log N(\text{O II})$ (cm^{-2})
(1)	(2)	(3)	(4)	(5)	(6)	(7)	(8)	(9)
37	0.37771	13.79 ± 0.12	0	< 13.38	-1	-0.24	13.68	13.37
38*	0.37845	14.49 ± 0.08	0	< 13.78	-1	-0.20	14.51	13.16
40	0.38233	14.02 ± 0.09	0	< 13.42	-1	-0.24	14.03	13.25
42	0.38759	14.83 ± 0.13	-2	< 14.11	-1	-0.30	14.81	14.10
43	0.40936	14.28 ± 0.09	0	< 13.59	-1	-0.52	14.21	13.58
49*	0.42079	13.77 ± 0.09	0	< 13.74	-1	-0.31	13.67	13.80
51*	0.42731	14.71 ± 0.08	0	< 13.91	-1	+0.20	14.66	14.05
55*	0.44609	14.37 ± 0.03	0	< 13.45	-1	-0.70	14.23	13.47
59	0.48168	14.17 ± 0.04	0	13.54 ± 0.10	0	-0.78	14.16	13.50
61	0.49450	13.52 ± 0.08	0	< 12.98	-1	-0.78	13.47	12.97
62	0.49888	14.25 ± 0.09	0	< 13.85	-1	-0.24	14.21	13.80
67	0.53351	14.50 ± 0.21	-2	14.12 ± 0.27	0	-0.33	14.50	14.12
68	0.53459	14.25 ± 0.15	0	< 13.69	-1	-0.75	14.23	13.68
73	0.55647	14.53 ± 0.17	-2	< 13.87	-1	+0.38	14.44	13.94
74	0.55753	14.75 ± 0.04	-2	< 13.68	-1	-0.18	14.73	13.68
78	0.57649	13.89 ± 0.16	0	< 13.64	-1	-0.15	13.90	13.63
82	0.59956	14.38 ± 0.01	0	14.05 ± 0.02	0	-0.08	14.41	14.06
84	0.61025	14.31 ± 0.05	0	< 13.57	-1	+0.04	14.31	13.41
85	0.61566	14.59 ± 0.03	-2	13.54 ± 0.08	0	-0.20	14.54	13.56
87	0.61913	15.18 ± 0.03	-2	< 13.47	-1	-0.36	15.13	13.44
95	0.68895	14.90 ± 0.04	-2	< 13.86	-1	-0.42	14.86	13.83
97	0.71896	14.04 ± 0.10	0	< 13.66	-1	-0.23	13.96	13.65
98	0.80775	14.41 ± 0.02	0	< 13.29	-1	-0.49	14.41	13.24
99	0.82917	13.42 ± 0.09	0	< 13.15	-1	-1.37	13.45	12.93

Note- Col ID: (4) Flag in the column density measurement of O III (6) Flag in the column density measurement of O II. Flag '0' indicate detections whereas '-2' and '-1' indicate lower limits and upper limits, respectively.